Paleolimnological implications of Late Holocene sediments in the western Sea of Galilee, Israel

A THESIS
SUBMITTED TO THE FACULTY OF
UNIVERSITY OF MINNESOTA
BY

Abigail M. Williams

IN PARTIAL FULFILLMENT OF THE REQUIREMENTS
FOR THE DEGREE OF
MASTER OF SCIENCE

Dr. Emi Ito

March 2016

Acknowledgements

There have been many people who had a hand in helping me complete the work presented here.

To start, I thank Hadar Elyashiv of the Geological Survey of Israel for help with some grain size analysis, Daniel Palchan and Michal Ben Israel for assistance in the isotope lab at the Hebrew University of Jerusalem, Israel-Ramat Gan, Michael Kitin and Yaacov Mizrachi for driving us to, from, and all around the lake and for assisting in sample retrieval, Oz Dar Tsabari for taking us out on the lake to collect sediment, the Kinneret Lab for providing space to work and sharing data, Johnathon Laronne and Noa Hillel from Ben Gurion University for obtaining Amud and Tsalmon discharge data, Chris Paola for discussion about sedimentary fabric of the core and, in particular, the flood deposits, Kristina Brady and Jess Heck for assistance in the LacCore Core Laboratory, and Vania Stefanova and Amy Myrbo for assistance with the age-depth model.

I also thank Ahuva Almogi-Labin and Moti Stein for field assistance, their expertise and opinions on the project, and helping me feel at home in Israel by showing me how to shop at the Mahane Yehuda market in Jerusalem, sharing Shabbat, countless historical tours, and hosting Emi and myself on multiple occasions. Without their generosity, my stays in Jerusalem would have been impossible and, therefore, I would not have been able to accomplish the work I did.

I must also thank two people who brought me pizza when I needed it most: Megan Korchinski and Daniel Palchan. Megan sent me (too much) pizza while I was

working late hours with Emi preparing my thesis and defense, which was really unexpected considering she was in Australia working on her own research. Daniel brought me pizza and beer when I had to stay over night at the hospital in Jerusalem for observation after getting concentrated HF on my face while working in the isotope lab. That was the only time I've ever stayed at a hospital, let alone in another country, so pizza was a welcome sight.

I thank my committee members David Fox and Amy Myrbo for their time and input on my thesis and for providing their perspectives on this multifaceted project.

Lastly, I thank my adviser Emi for all of the time she spent helping me write and edit my thesis, her confidence in my abilities, and her patience. This is a cliché, but it is difficult for me to find the words to express my gratitude for how supported I felt throughout my graduate experience. Simply put, I am certain finishing my MS would not have happened without Emi and I don't think I can thank her enough.

Dedication

To my family and friends who helped me cross the finish line.

Abstract

A 143-cm UWITEC percussion core, collected from a water depth of ~10 m, about 1 km from the city of Ginosar on the western shore of the Sea of Galilee, was studied to infer input from East Galilee over the last ~4000 years. The core location is offshore the mouths of Amud and Tsalmon, two of the larger streams that drain the northeastern part of the Galilee Mountains and have formed Holocene alluvial deposits. Today these streams are seasonal and during some years have no flow. Changes in core lithology, grain size, elemental chemistry, and bulk carbonate-free $^{87}Sr/^{86}Sr$ ratios and ε_{Nd} values indicate changes in lake levels and sediment delivery from the Galilee. The presence of mm- to cm-thick laminations in the bottom 20 cm of the core indicate that the lake was deeper than today from ~4000 to ~3500 cal yrs BP and became shallower reaching near modern depth by ~3250 cal yrs BP. Summertime daily afternoon windwaves caused by westerly wind coming across the Galilee Mountains creates counterclockwise gyres and sediment resuspension to the depth of about 10 m resulting in accumulation of massive sediments in zones shallower than ~10 m (Serruya, 1978). Two thick flood units were identified, one on top of the other, between 104 and 60 cm. Both show a fining upward trend. The earlier flood shows lithology and $^{87}Sr/^{86}Sr$ ratios and ε_{Nd} values similar to Amud drainage basin rocks and soils whereas the later flood shows affinity to Tsalmon drainage basin. Additional minor sediment delivery events are suggested by the presence in the sediment of Late Cretaceous to Eocene marine foraminifer fossils that are known to occur in carbonate rocks and their weathering products (Terra Rossa and Rendzina soils)

exposed in the Galilee Mountains. An event that resulted in a hiatus occurred sometime between ~530 and ~1200 cal yrs BP.

Table of Contents

List of Tables

List of Figures

Chapter 1. Introduction

Motivation for the study

The Sea of Galilee, the major source of freshwater in Israel, is located in the Kinnarot Basin, which is one of the morphotectonic depressions along the Dead Sea Transform (Fig. 1.1).

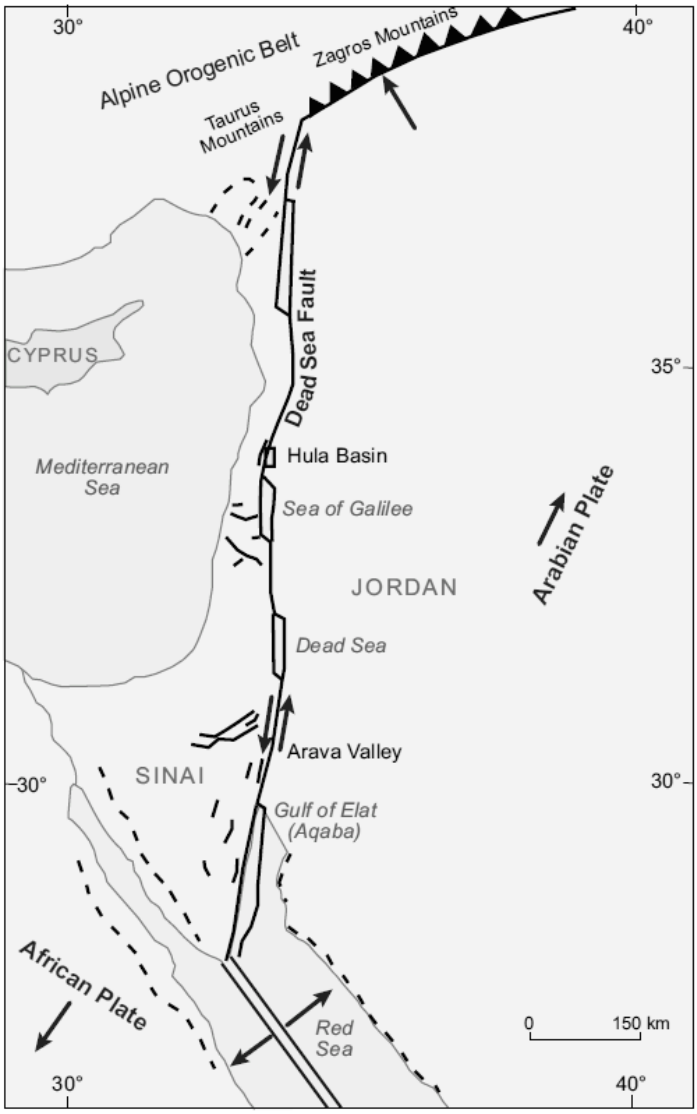

Figure 1.1. Diagram of Dead Sea Transform Fault (Ben Avraham et al., 2014).

Today, the Sea of Galilee gets its water mainly from the Jordan River contributing about 2/3 of the fresh water to the lake (Flexer et al., 2000), and whose tributaries, the Dan, Banias and Hazbani are fed by winter rains and Mt. Hermon's aquifers. Additional inputs come from rainfall on the Golan Heights and East Galilee (Flexor, et al., 2000) which contribute water to several small streams and aquifers of carbonate and basaltic lithologies, some of which discharge as saline springs along the western coast of the lake. Possible occurrences before the mid-20th Century of significant sediment delivery or water discharge events from streams originating in East Galilee have received little attention since most of inflow comes from the perennial Jordan River and a few other streams such as Meshushim draining the central Golan. Hula Basin marsh, before it was drained in the 1950s for agricultural purposes (Gophen, 2011), trapped most of the sediment being carried by Jordan and its tributaries. Studies of the Sea of Galilee sediment have mainly focused on endogenic carbonate precipitation or fine particles (Singer et al., 1972) associated with algal blooms and nutrient cycling or atmospheric deposition (Ganor et al., 2000; Koren & Klein, 2000; Gross et al., 2013). Today, streams draining East Galilee such as Amud and Tsalmon are dry or nearly so most of the time (Israel Hydrological Survey database, Israel Water Authority, Jerusalem). However, a strong Cyprus low-pressure system should bring more rain to the Galilee Mountains, as it does to the Judean Mountains and to parts of the Negev Desert (Enzel et al., 2003; Haliva-Cohen et al., 2012), so that strong water-sediment discharge events should have occurred in the past. The Cyprus low-pressure system creates a counter-clockwise wind rotation over the eastern Mediterranean region (Fig. 1.2) that brings moisture over the

Saharan and Arabian-Nubian Shields resulting in increased dust deposition in the Kinnarot Basin. Erosion could have been enhanced by human activities increasing sediment load (Baruch, 1986; Langutt et al., 2013, 2015; Schiebel, 2013).

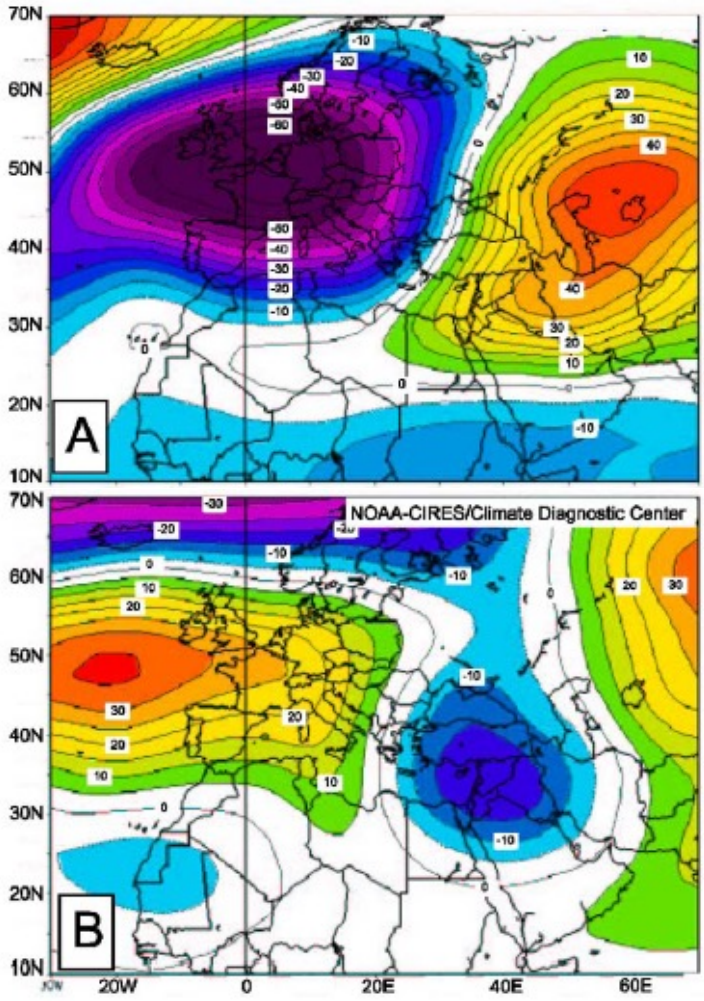

Figure 1.2.
Map of high and low pressure systems over the Mediterranean region. Map A shows the Cyprus high pressure system and map B shows the Cyprus low-pressure system that causes wet conditions in the Kinnarot Basin.

Agriculture and deforestation increased between 2500 cal BP and 1000 cal BP (Baruch, 1986), which would have provided increased erosion of soil from the catchments into the valleys. Rain events over the East Galilee Mountains would then deposit the material in the Sea of Galilee at an accelerated rate caused by Roman use of the land.

To investigate occurrence of increased precipitation periods and events in the East Galilee, six cores were taken from the Sea of Galilee. The focus of this project is a 143 cm core (LK12_22) with a basal age of ~4000 cal BP collected offshore Ginosar near the mouths of the Amud and Tsalmon streams in 2012. The Amud and Tsalmon enter the Sea of Galilee approximately 1 km from LK12_22 core site. The discovery of significant flood events originating in the Galilee Mountains and their timing may be tied to Roman and Byzantine Period humans who lived in the area (Dark, 2013). This study focuses on the sediments of the last ~4000 years and complements another study on the ostracode species assemblage from the same core.

Chapter 2. Materials and Methods

Study Area

The Sea of Galilee is located in the Kinnarot basin, a pull-apart basin of the Dead Sea Transform Fault (Fig. 1.1). Movements across the Dead Sea Transform Fault created a series of such basins, which filled with seawater during the Miocene (Garcia-Veigas et al., 2009). The lake level elevation averages about 210 m below mean sea level (Berman et al., 2014). The present day Sea of Galilee has a maximum depth of 46 m and surface area of 167 km^2. There are significant seasonal and interannual variations in the lake level and thus the surface area. Daily westerly winds from the Mediterranean Sea occur from April through September caused by daytime heating of the Galilee region giving rise to large strong waves that may mix and transport shallow sediments above wave base (Alpert et al. 1982; Avissar & Pan, 2000; Imberger & Marti, 2014). The winds begin at Noon and last 8-12 hours resulting in counterclockwise circulation of surface waters in the northern three-fourths of the lake (Pan et al., 2002). During the windy season the upper layers of water are continuously mixed, which establishes a strong temperature gradient forming anoxic bottom water that becomes thicker during the summer (Imberger & Marti, 2014).

The northern part of the Sea of Galilee catchment (northern Golan, and Hermon units, Rimmer & Givati, 2014) receives winter precipitation ranging from 1600 mm/yr in the highest elevation to 600 mm/yr closer to the lake, which accounts for about half of the Jordan River's baseflow (Fig. 2.1) (Goldreich, 1995; Nishri et al., 1999; Singer, 2007). In lower elevation sites near the lake and on the lake itself, mean annual precipitation varies

from 400 to 600 mm/yr (Goldreich, 1995). In areas north of the Sea of Galilee, summer and winter temperatures are largely a function of elevation, with low elevation sites near the lake averaging 30°C in July and 13°C in January, and higher elevation sites (>400 m amsl) averaging 25°C or lower in July and below 10°C in January (www.ims.gov.il/IMSEng/CLIMATE).

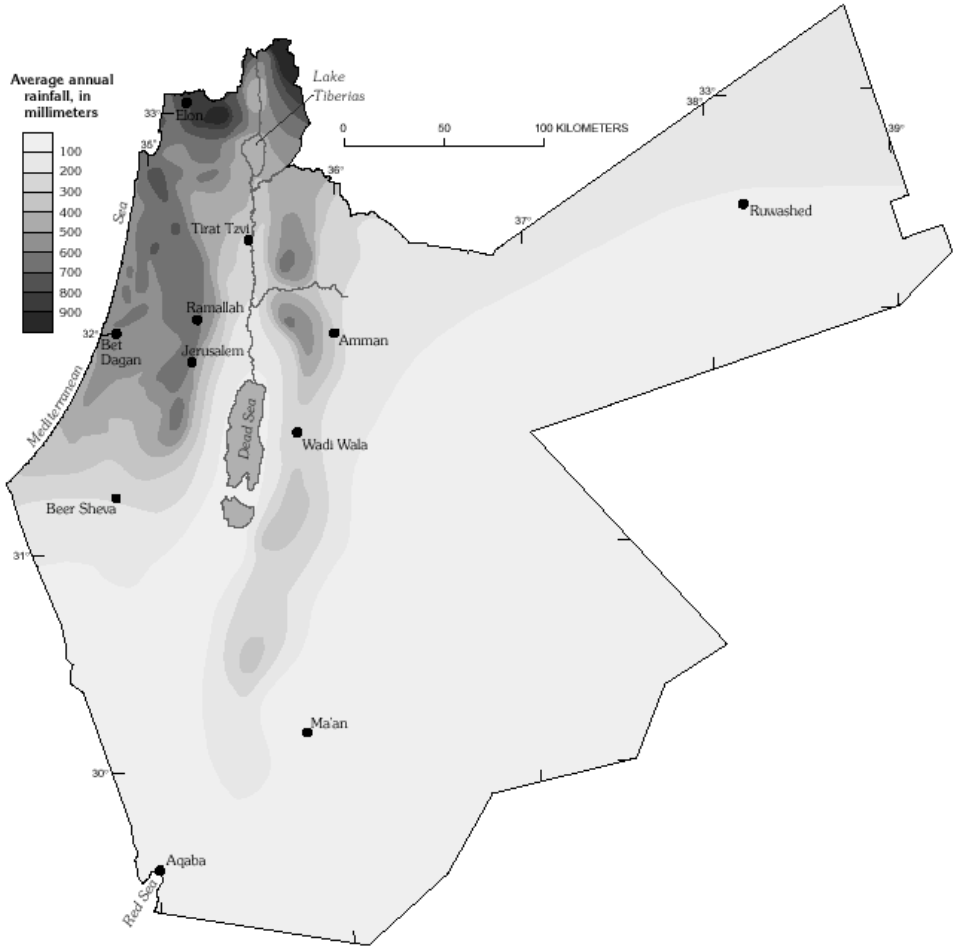

Figure 2.1. Annual rainfall for the Jordan River Valley and surrounding deserts and highlands (Overview of Middle East Water Resources, USGS, 1998).

Onshore and underwater fresh and saline springs enter the lake mostly on or near the western side of the lake (i.e., Tabha, Fuliya, Hamei Tiberia, Ma'agan and the Barbutim

Group springs, 1,700-31,000 mg/L). The discharge rates from these springs are positively correlated with increased precipitation over low-elevation southeastern portions of the Galilee because a higher hydraulic head forces stored saline water to discharge along various faults that are part of the Dead Sea Transform system (Gvirtzmann et al., 1997).

The focus of this study is the East Galilee, the mountains of the Lower Galilee that drains toward the Sea of Galilee. Occasionally, there are rain events on the East Galilee (Rimmer & Givati, 2014) that drain through wadis such as Amud and Tsalmon near the city of Ginosar. Due to translation from Hebrew to English, there are several English spellings of Tsalmon (e.g. Zalmon that appear in Figure 2.2). The Amud catchment is longer and reaches a higher elevation than the Tsalmon, which experiences a higher rate of weathering and dissolution to the local carbonates due to the greater volume of rainfall at higher elevations in the East Galilee. The Amud catchment is rich in Terra Rossa soils and ample Fe III is available, while the Tsalmon catchment has more Rendzina soils, which are less weathered and contain more Fe II. The oxidized Fe III gives Terra Rossa soils their characteristic brick red appearance whereas the Rendzina soils maintain a dull gray color.

Aside from Aeolian deposition, endogenic carbonate precipitation, and some sediment possibly transported to the area by the Sea of Galillee's bottom current, these seasonal streams may have provided a significant amount of sediment for this region of the lake before their waters were appropriated for irrigation in the mid-20th Century.

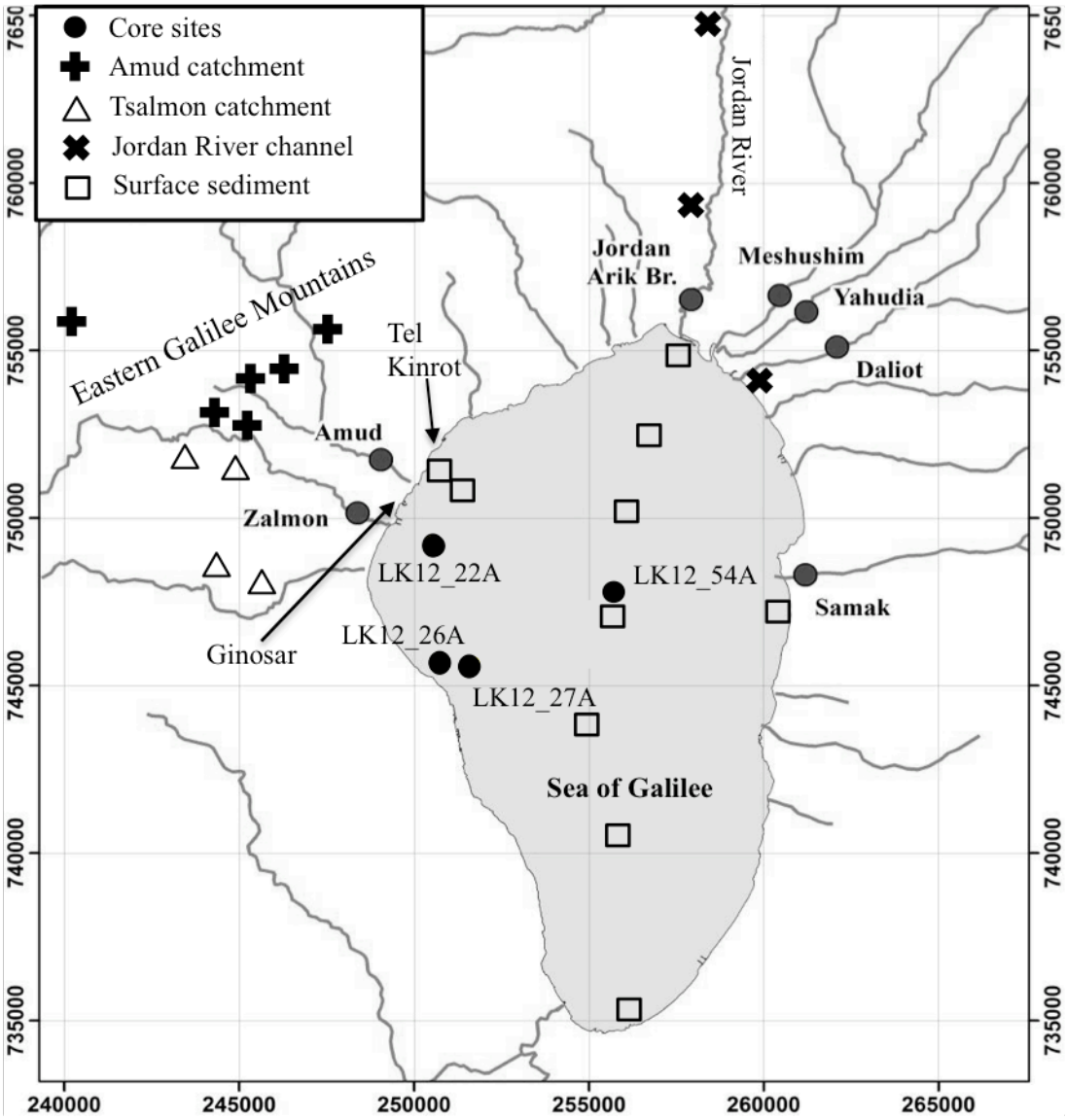

Figure 2.2. Sample locations and stream locations for the Sea of Galilee. Dark gray circles represent stream stations. Original map from the Hydrological Survey of Israel Annual Report.

The drainage basin of Amud is oriented in the northwest direction from Ginosar and headwater areas include Mount Meron at 1208 m amsl. The drainage basin of Tsalmon is oriented East-West with the mouth in Ginosar with the highest headwater elevation of 602 m at Mount Kamon. The Amud drainage basin receives higher annual

precipitation (>900 mm/yr at Mount Meron area; Goldreich, 1995) due to its higher average elevation compared to the Tsalmon drainage basin, which receives 400-600 mm/yr (Goldreich, 1995). This difference is reflected in the higher annual discharge for Amud (Reichman et al., 2014). The alluvial fans at the mouth of the wadis join together at the Sea of Galilee and comprise a broad coastal valley ~5 km wide where the fan intersects the lake and ~2 km from the coast to the apex of the fan.

The geology of both catchment basins is dominated by Late Cretaceous and Eocene age limestones, dolostones, chalks, and marls with some Pliocene age basalt. These carbonates contain fossils of several benthic and planktonic species of marine foraminifers. Both wadis show evidence of massive erosion with the presence of canyons, lapies, and landslide deposits. The bedrock is overlain with Terra Rossa and Rendzina soils (Soil Map of Israel, Geological Survey of Israel).

There have been several engineering efforts in the last century to both manipulate where the fresh lake water is held and to decrease the saline water input from springs. The National Water Carrier was installed in 1964 to pump fresh water out of the Sea of Galilee to the Eshkol Reservoir and saline springs were diverted to the Lower Jordan River, which caused a dramatic decrease in the chloride concentration of the lake (Naser, 1998). It is estimated that the National Water Carrier today removes more water from the lake (~300×10^6 m^3/yr), than is likely lost through evaporation (~230×10^6 m^3/yr) (Rimmer & Givati, 2014).

Core acquisition

Cores 21, 22, 23, 26, 27, and 54 were collected from various locations around the Sea of Galilee in 2012 with a UWITEC hammer corer fitted with a PVC liner tube. They are labeled as LK12_XX, where XX is the core number, in Table 2.1. The core locations around the Sea of Galilee ranged from the northwestern littoral region, near shore, and central basin of the Sea of Galilee (Fig. 2.2; Table 2.1). After each core was acquired, to prevent the sediment from being disrupted during transportation, the empty space at the top and bottom of the liner tube was filled with blocks of floral foam. All cores except LK12_22 were shipped to the National Lacustrine Core Facility (LacCore) at the University of Minnesota for initial core description and archiving. Core LK12_22, the subject of this study, was shipped to the Free University of Berlin for a detailed ostracode study (Williams, et al., in prep.). One longitudinal half remains in Berlin and the other half was shipped to LacCore.

Table 2.1.
Core IDs, coordinates, and field notes taken from the Sea of Galilee in 2012.

Core ID	Location (lat., long.)	Water Depth (m)	Sediment Length (cm)
LK12_21	+32.85467, +35.54372	12.0	150.0
LK12_22	+32.83861, +35.53373	11.0	143.0
LK12_23	+32.83229, +35.52937	10.0	149.0
LK12_26	+32.80921, +35.53009	10.0	151.5
LK12_27	+32.81234, +35.53904	15.0	60.0
LK12_54	+32.82379, +35.60701	39.6	44.0

Surface samples

Surface-sediment samples were collected from the lake bottom in June 2012 and June 2013, and sediments from springs and the Jordan River bottom in June 2013 (Table 2.2). Lake surface-sediment samples were collected using an Ekman dredge and stored in Whirl-Pak® bags. In general, the on-shore sediment from springs was collected as a grab sample from the discharge point of springs when they could be located or from near the center of a spring pool or in the outflow channel using a nylon coffee filter or a custom built "bola" sampler. Sediment samples from rivers were generally collected from quieter vegetation-protected areas near the bank. The "bola" sampler is a 5 cm diameter metal pipe with a 150 μm mesh bottom attached to a 11.5 m long rope that is tossed into the water, allowed to sink, dragged a short distance to gather sediment, and then pulled out of water.

Table 2.2.
Lake surface-sediment sample IDs, coordinates, and field notes.

Sample ID	Location (lat., long.)	Water Depth (m)	Site Remarks
LK1	+32.88575, +35.60892	5.0	Near Jordan River mouth
LK7	+32.86572, +35.60453	22.0	~2.4 km south of Jordan River mouth
LK9	+32.85229, +35.60007	27.0	~4 km south of Jordan River mouth
LK10	+32.82104, +35.58897	32.0	Center of lake
LK12	+32.77697, +35.57550	27.0	West central part of lake
LK15	+32.74557, +35.57742	19.0	South central part of lake
LK17	+32.72895, +35.59735	12.0	South central part of lake
LK41	+32.72511, +35.61354	8.0	South near shore
LK46	+32.81178, +35.64328	10.0	Central eastern near shore
LK105	+32.89088, +35.61959	0.1	Jordan River, ~800 m from lake
LK122	+33.01076, +35.62846	0.2	Upper Jordan River
LK125	+33.19597, +35.62637	0.5	Upper Jordan River
LK126	+33.24747, +35.65095	0.3	Upper Jordan River
LK159	+32.84341, +35.53203	10.0	550m N of LK12_22
LK161	+32.84521, +35.52995	6.0	800m N of LK12_22

Soil samples

Additional surface sediments were taken from the Ginosar Valley in May 2015 (Fig. 2.2; Table 2.3). Approximately 100 g of soil was collected using a trowel and stored in a plastic bag under ambient temperature.

Table 2.3.
Soil sample IDs, coordinates, and field notes.

Sample ID	Location (lat., long.)	Depth (cm)	Site Remarks
S Rvd 1	+32.84601, +35.45997	0	Tsalmon catchment, surface with some rain drop marks
S Rvd 2	+32.84601, +35.45997	10	Tsalmon catchment
S Rvd 3	+32.84601, +35.45437	10	Tsalmon catchment, contact with *in situ* rock
S Rvd 4	+32.84601, +35.45437	0	Tsalmon catchment, surface
S Amud 1	+32.86891, +35.50239	0	Stream channel, Amud catchment
S Amud 2	+32.86891, +35.50239	0	Terrace 50 cm above stream bottom, Amud catchment
S Huk 1	+32.89395, +35.48565	5	W of Hukok kibbutz, hole under Ella tree
S Huk 2	+32.87526, +35.48565	0	Above basalt quarry in contact with broken basalt
S Khl 1	+32.88651, +35.51016	0	Southern point of Kahal moshov
S Haz	+32.89917, +35.40278	5	Mt. Hazon, southern slope under fire post

Initial core description

At LacCore split cores were analyzed for point magnetic susceptibility with the Geotek MSCL-XYZ and imaged with the Geotek Geoscan-III. The Geoscan-III uses a line-scan CCD camera with polarizing filters to prevent any glare from the wet sediment. Images are scanned at 20 pixels/mm. During visual lithologic description, some smear slides were made and examined under 100x petrographic microscope using plane- and cross-polarized lights. Smear slides were made from visually distinct portions of the cores to examine minerals, aquatic organisms, terrestrial plant remains, and any other material contained in the sediment. A toothpick was used to extract a minimal amount of sediment from the center of the split core and spread on a microscope slide. A drop of deionized water was added to the smeared sediment and after drying, a few drops of Norland 21 optical cement was added and slip cover was placed to protect sediment. Optical cement was cured under an ultraviolet light.

Chronology

The chronology was determined by radiocarbon dating of charcoal picked from nine depths throughout the core. We extracted ~1 cm^3 of sediment from a thickness of 0.5 cm and washed this aliquot through a 125 μm sieve using doubly deionized (DDI) water. The material remaining in the sieve was suspended in DDI water in a picking tray. Using a binocular microscope and tweezers, the wet charcoal was picked and stored in 2 dram glass vial, previously burned for 4 hours at 550^{o} C to remove any organic carbon, partially filled with DDI water and several drops of 10% HCl to prevent the growth of

mold and preserve the integrity of the charcoal. If there was an insufficient amount of charcoal from the initial picking, an additional ~1 cm^3 of sediment from the original sample depth was processed. If there was not enough sediment left from the original depth, samples were taken from above and below the original interval. The overall sampled interval never exceeded 2 cm in thickness in an attempt to maintain the precision of the age determination.

The charcoal samples were sent to the Lawrence-Livermore National Laboratory's Center for Accelerator Mass Spectrometry (CAMS). These results were calibrated using Calib 7.1 (Stuiver et al., 2005) and Bacon, a Bayseian age-depth model (Blaauw & Christen, 2011), which both use IntCal13.

XRF and X-radiography

A COX Analytical Systems ITRAX XRF Core Scanner at the Large Lakes Observatory, University of Minnesota, Duluth, was used to obtain elemental composition and X-radiographic images on split cores at a maximum resolution of 200 μm. For XRF, a 1 cm wide central swath of the split core section was scanned and measurements were taken every cm-. The elements focused on for this study are Fe, Mg, Ca, and Mg. The X-radiographic images were taken at 200-micron resolution (5 pixels/mm or 127 dpi) after the XRF scan on the same 1 cm wide swath.

XRD

Several sediment samples from core LK12_22 were chosen from portions of the core with lithological changes and analyzed with a Rigaku Miniflex XRD. The sediment is

ground to a fine powder (<63 μm) with DDI water and a corundum spike and pipetted onto a slide before analysis. Once the samples were run, the program Jade was used to identify the possible minerals present and their abundance (the weight percent).

Grain Size Analysis

About half of the Core LK12_22 samples were analyzed at LacCore and the rest were processed at the Geological Survey of Israel. The bulk sediment was sampled at LacCore. The analysis at LacCore and at the Geological Survey of Israel involved pretreatment (http://lrc.geo.umn.edu/laccore/procedures.html). Any isolated and visually unique grain size segments were sampled separately to prevent obscuring size distribution of each segment. Pretreatment begins with ~5 cc of sediment taken from continuous 2 cm thick intervals. Organic matter is removed by several rounds of dissolution with 30% H_2O_2, and biogenic silica dissolved with 1M NaOH, and the remaining slurry is neutralized with a small amount of 0.5N HCl. Then the samples are centrifuged at 3500 rpm for 5 minutes and rinsed with deionized water. The rinsing and centrifuging is repeated three times. The remaining material is combined with a sodium hexametaphosphate solution (5 g Na-HMP to 1L DDI water) prior to analysis. Grain size analysis at LacCore uses a Horiba Grain Size Analyzer LA-920. The Horiba autosampler at LacCore holds 12 samples, and 4 samples are selected at random for a duplicate analysis to check for consistency throughout each run. The Geological Survey of Israel uses a Malvern Mastersizer Hydro MU 2000.

$^{87}Sr/^{86}Sr$ and $^{143}Nd/^{144}Nd$ Analysis

The analyses of $^{87}Sr/^{86}Sr$ and $^{143}Nd/^{144}Nd$ of the core and surface sediment samples used the method described by Ben Israel, et al. (2015) at the Geological Survey of Israel using Nu Instruments MC-ICPMS and at the Hebrew University of Jerusalem using Neptune™ MC-ICP-MS. Sr and Nd isotopic ratios were corrected using NIST SRM 987 standard for Sr ($^{87}Sr/^{86}Sr = 0.71025$; Ehrlich et al., 2001) and JNdi standard for Nd ($^{143}Nd/^{144}Nd = 0.512115$; Tanaka et al., 2000). To account for a possible analytical shift, isotopic ratios were corrected based on $^{86}Sr/^{84}Sr = 0.1194$ and $^{146}Nd/^{144}Nd = 0.7219$ (Lugmair et al., 1975). Repeated measurements of the standards yielded $^{87}Sr/^{86}Sr$ (NIST SRM 987) = 0.71029 (2σ= 5.11E−5; n = 37) and $^{143}Nd/^{144}Nd$ (JNdi) = 0.51209 (2σ = 1.36E−5; n = 27). $^{143}Nd/^{144}Nd$ ratios are reported as ε_{Nd}, which is the corrected measured $^{143}Nd/^{144}Nd$ ratio normalized to CHUR ($^{143}Nd/^{144}Nd = 0.512638$; Jacobsen & Wasserburg, 1980).

Foraminifer fossils

The core LK12_22 at the Free University of Berlin was sampled for another study (Williams et al., in prep.). The sediment was sieved in alternating continuous cm-thick subsamples. While picking ostracode shells for a species assemblage and shell chemistry study (Williams et al., in prep.), the presence of fossil marine foraminifers was noted.

Chapter 3. Results

Core description

Core LK12_22 was divided into 6 units based on sediment characteristics (e.g. grain size, texture), scanner XRF results, radiocarbon ages, and smear slide observation (Fig. 3.1). The prominent characteristics are described below and shown in Figures 3.2, 3.3, 3.4, 3.6 and 3.7. The core was cut into two segments at 63 cm, which created a small gap in some analyses just above and below this depth.

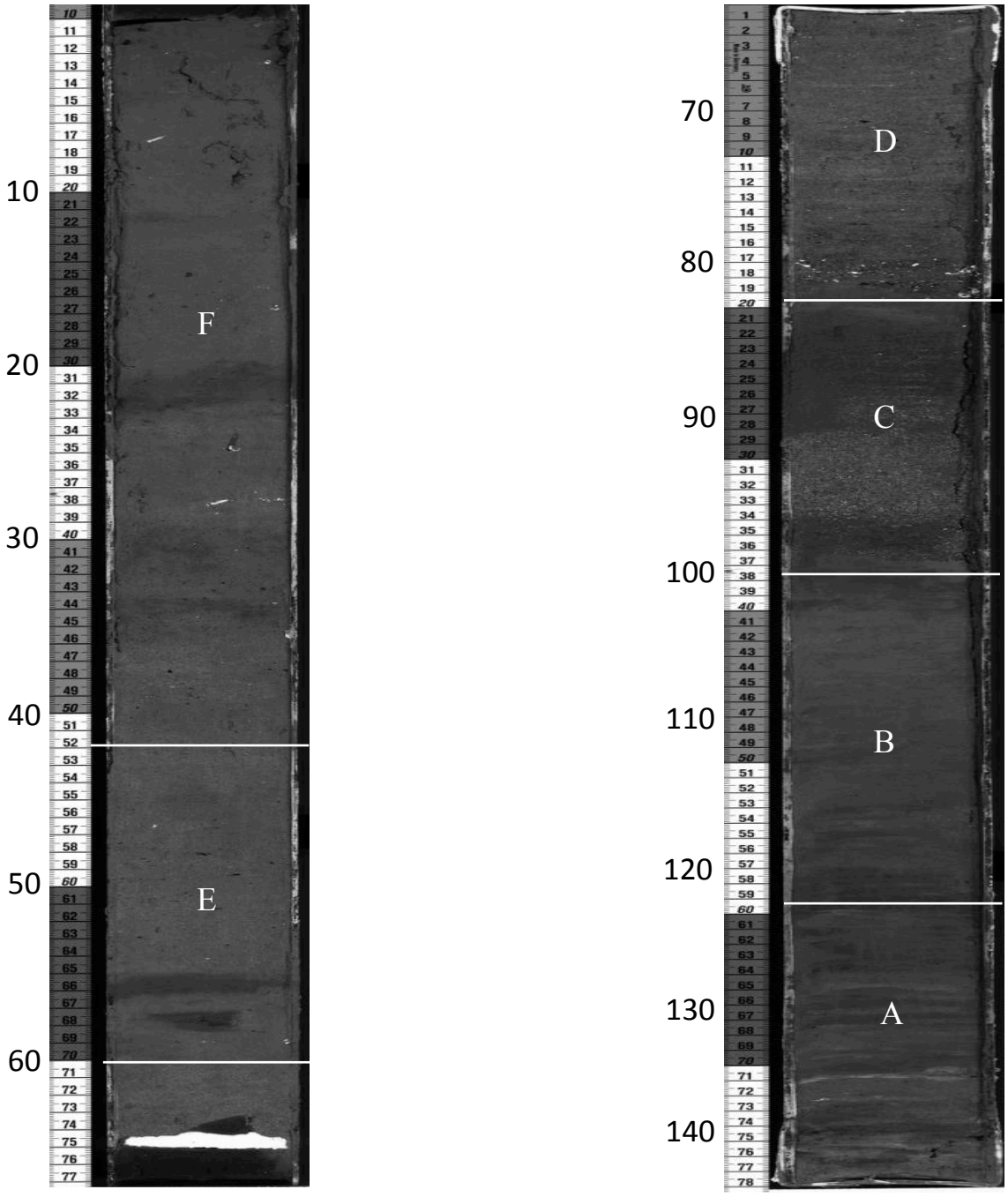

Figure 3.1. Scanned image of core LK12_22 showing unit boundaries. The corrected depth of core sediment is shown to the left of the core images.

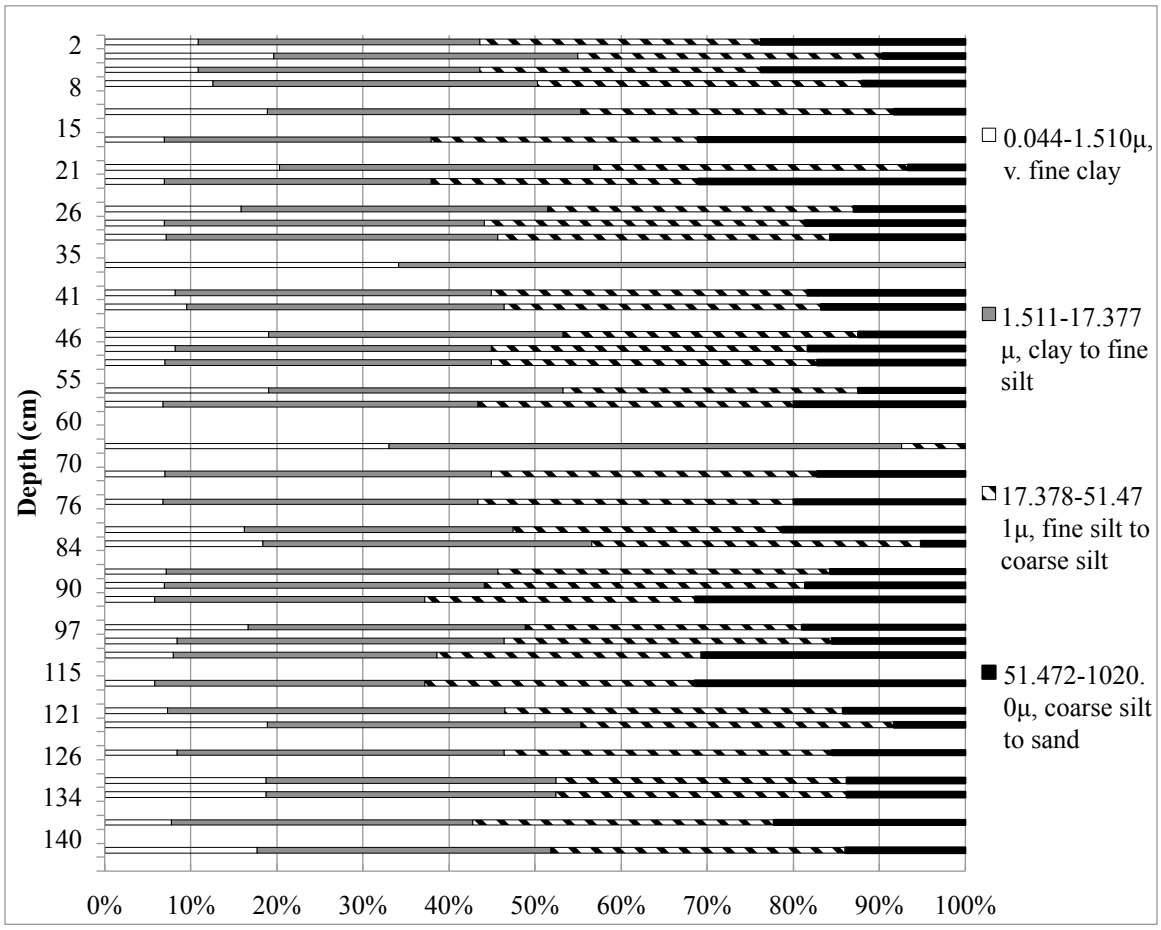

Figure 3.2. Grain size analysis of core LK12_22.

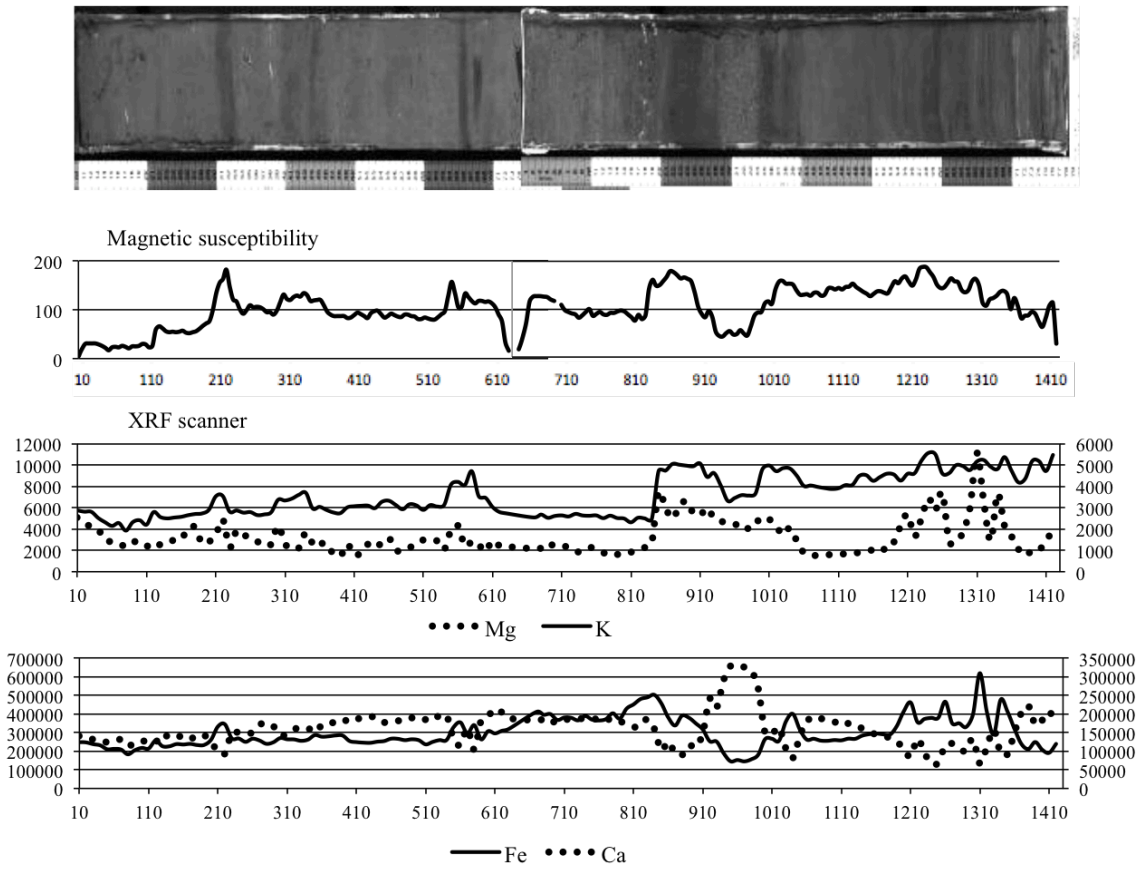

Figure 3.3. Magnetic susceptibility and XRF scanner results to scale with core image.

Unit A (143-122 cm) is characterized by laminations gradually decreasing in color contrast up core. Alternating randomly between dark brown, reddish taupe, brownish red, and cream colored sediment, the lamination thickness ranges from mm- to cm-scale with no apparent grain size gradation throughout the entire section. One exception at 137 cm is a cm-thick sandy package with broken shells at its base. Most of the unit is subequal parts fine silt to coarse silt with ~15% sand until 137 cm, where there is an increase to 25% sand-sized sediment. Magnetic susceptibility increases up core in Unit A with high values coinciding with increased scanning XRF Fe spectral intensities.

Fe and Mg intensities show peaks at 140, 134, 131, 126 cm and low values at 138, 133, 127, and 122 cm. Ca show peaks at 141, 138, 133, 130, 126 cm and decreases at 142, 139, 135, 131, 129, and 124 cm. K increases at 135, 133, 128, and 126 cm. All elements vary in fluorescence intensities corresponding to laminations in this unit. In general, the darker sediment coincides with increased Fe, Mg, and K intensities and lighter colored sediment occurs with increased Ca intensities. XRD analysis of bulk sediment from 130-128 cm shows that the major minerals are quartz, phyllosilicates, and calcite with minor dolomite.

Unit B (122-100.5 cm) is a massive reddish taupe unit with fossils at 108 and 106 cm. Grain size is about 5% fine clay, 80% silt, and 15% fine sand at the base, becomes coarser in the mid-section (116-111 cm) with 30% fine sand, and returns to the same sandy silt grain size distribution as between 122-116 cm by 100.5 cm. Fe and Mg give high fluorescence intensities at 121 and 104 cm with consistently low intensities between 118-106 cm. K follows the same low intensity pattern and increases at 106 cm. Ca has minima mirroring Fe and Mg maxima, gradually increases from 118-106 cm, and peaks at 102 cm. XRD analysis on bulk sediment from 110-108 cm showed mineralogy dominated by quartz and calcite with minor phyllosilicate, dolomite, and plagioclase.

Unit C (100.5-83 cm) is a red upward fining segment with continuous presence of fossilized foraminifers. The boundary between the Units B and C show an abrupt change in grain size and color. Magnetic susceptibility decreases throughout the sandy layer from 97-91.5 cm and increases for the remainder of the section to 83 cm. The X-radiography shows persistent fine mm-scale laminations not observable by the naked eye. From

100.5-97 cm, there is a sandy section with ~2-mm thick layer of fine sediment at 97 cm. A silty sand (32%) is present from 97-91.5 cm. Above 91.5 cm the sediment becomes finer until 83 cm (5%). The upper boundary of Unit C is not oriented parallel to the core bottom, but is curved concave upward, distinct from a coring artifact which are typically concave downward. The unit boundary is ~1 cm deeper on the right side relative to the left. Grains viewed in a smear slide generally have angular geometry throughout this unit. Fe intensity peaks at 100 cm, decreases from 99.5-93 cm and increases until 83 cm with a brief decrease at 87 cm. Mg and K follow a similar pattern as Fe with a little finer scale variation. Unlike other segments in the core where Fe and Mg covary, at 100 and 93 cm, Mg decreases while Fe increases. Overall, Ca decreases where Fe increases and *vice versa* until the top of the unit where both show an increase. Sediment analyzed for XRD throughout the unit showed that the coarsest segment (98-95 cm) was mostly quartz and calcite. XRD analysis of sediment taken from 90-88 cm shows high concentrations of quartz and phyllosilicates in addition to minor calcite and dolomite. XRD results from 86-85 cm were mainly calcite, quartz, and plagioclase with minor dolomite.

Unit D (83-60 cm) is another fining upward segment with a 1.5 cm-thick layer of broken and whole shells of freshwater gastropod, *Melanopsis*, at the base and foraminifer fossils at 83 and 76.5 cm (Fig. 3.4). The boundary between Units C and D has an abrupt change in grain size and lithology. The remainder of the section appears to have very little organized sedimentary fabric (e.g. lamination) in X-radiography or by visual inspection. Unit D is unlike the rest of the core because it is brownish gray and lacks the reddish color commonly observed elsewhere. It also lacks charcoal >125 μ, which is

found throughout the rest of the core. Grain size analysis of samples from 81.5-74 cm shows a slight decrease in sandy fraction until 69.5 cm, where the sediment is comprised entirely of fine clay (32%) and clay to fine silt (60%) and no sand. Magnetic susceptibility is steady until an increase from 70-64 cm. Fe and Mg intensities decrease up core to 79 cm and then gradually increases until 70 cm. Fe increases from 70-67 cm and decreases for the remainder of the section. Ca and K intensities are unchanging in the section until a decrease at 69 cm and an increase at 62 cm to the top. XRD results from 83-82 cm are primarily calcite and quartz with minor dolomite.

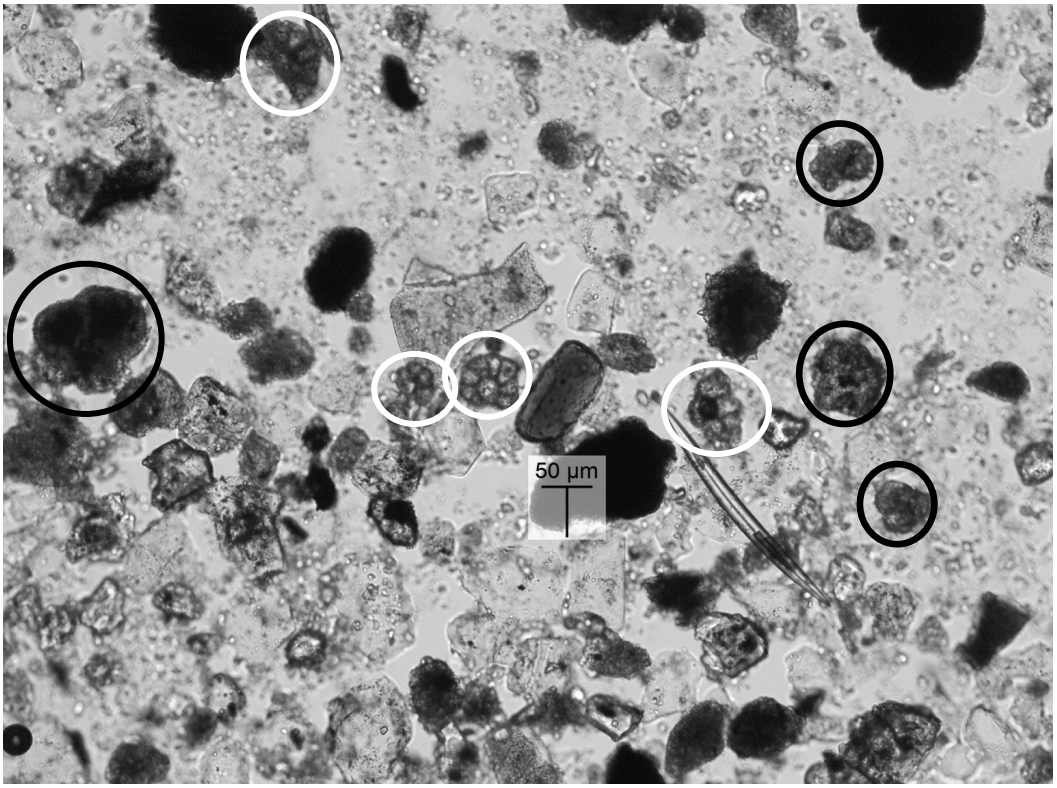

Figure 3.4. Smear slide from LK12_22, 77 cm. Benthic foraminifer fossils circled in solid white line and planktic foraminifer fossils circled in solid black line.

Unit E (60-42 cm) is predominantly a massive brownish gray unit with little visible sedimentary fabric. Foraminifer fossils are found at 51, 49, and 46 cm. Magnetic

susceptibility peaks at 59 and 56 cm and shows a generally decreasing trend with some variation between 56 and 42 cm. The grain size is predominantly a fine to coarse silt with no apparent gradation with depth. The distinct sedimentary features include a 1-cm thick and 3-cm wide dark brown angular bleb at 59 cm and an isolated brownish red 1-cm thick layer at 56 cm. The overall mottled appearance of the sediment is reflected in the X-radiography with no evidence of lamination. XRF-analyzed elements Fe, Mg, and K show peaks and Ca shows a valley at 59 and 56 cm. Fe intensities are slightly higher from 50-46 cm and lower from 46-42 cm. K intensities follow a similar trend until 42 cm where they decline for a 1-cm interval before increasing to the top of the section. Mg fluctuates with peaks at 53-51 cm, 46, 43 cm but intensities are overall lower between 54-42 cm. Ca values change slightly but the overall trend decreases up core. XRD analysis shows the major minerals are quartz and calcite for one sample at 56-55 cm and another at 52-50 cm.

Unit F (42-0 cm) is brownish gray with indistinct red layers from 34-30 cm, an isolated 2 cm thick red layer at 21 cm, a shell rich layer at 28 cm and foraminifer fossils at 32, 29, and 19 cm. Magnetic susceptibility peaks from 42-34 cm and 23-20 cm and continues to decline with a brief plateau at 12 cm. The average gain size for Unit F is clay to coarse silt. The percentage of sand-sized sediment is ~10% for most of the unit, but increases to ~30% at 24 and 16 cm. There is a fine-grained layer at 36 cm composed of fine clay to silt and a slight up core fining from 15-12 cm. In addition, there is a faint but distinct fine grained feature from 32-30 cm, comprised completely of fine clay to fine silt, that bifurcates from the fine silt down core for ~2 cm into the typical coarser silt. XRF

intensities fluctuate throughout this unit with Fe increasing from 42-30 cm, a significant peak at 22 cm for Fe, Mg, and K. Ca intensities decrease at all depths where Fe, Mg, and K increase. XRD results from the red layer at 32.5-30.8 cm produced quartz and calcite as major minerals in addition to phyllosilicates and dolomite as minor minerals. XRD on the sediment from 17-15 cm shows the major minerals to be quartz and calcite.

Chronology

The calibrated ^{14}C ages are listed in Table 3.1. Depths and calibrated ages increase relatively smoothly except for an age reversal and at 56 cm. Apparent sedimentation rates vary between ~0.07 cm/yr for the uppermost 43cm and ~0.02 cm/yr for 52-43 cm. The age-depth model produced in Bacon does not include the age from sample LK5 (Fig. 3.5).

Table 3.1.
LK12_22 ^{14}C ages and Calib 7.1 ages and Bacon 2.2 model ages. Calib 7.1 ages are used for all further discussion of the project.

Sample	CAMS number	Depth (cm)	^{14}C Age	Calib 7.1*	Bacon*
LK1	166565	18.5-19.0	275 ±35	360	144
LK2	166566	25.5-26.0	200 ±30	180	249
LK3	166567	34.5-35.0	335 ±40	390	404
LK4	166568	42.5-43.5	505 ±45	530	559
LK5	166569	51.0-52.5	1605 ±45	1480	**
LK6	166570	55.0-56.5	1300 ±70	1220	1109
LK7	166571	102.0-103.5	2240 ±100	2230	2533
LK8	166572	111.0-112.5	3060 ±60	3260	3033
LK11	166573	136.0-136.5	3605 ±40	3920	3884

*The most probable ages returned by Calib 7.1 and Bacon 2.2 are listed. **Sample removed by Bacon 2.2 before constructing the age-depth model.

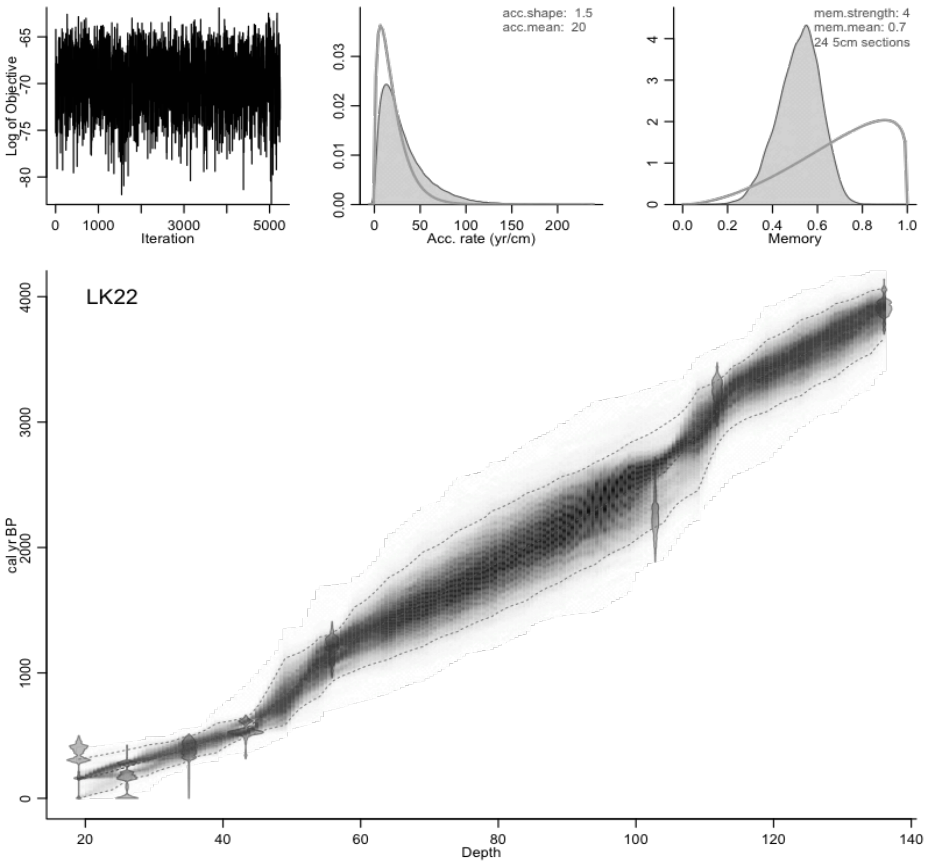

Figure 3.5. Bacon age-depth model for core LK12_22. Prior information, accumulation and memory, are shown above the model at their default values chosen by the program. The accumulation shape and mean were left at default values. The memory strength and mean define how much the accumulation rate at a specific depth of the core relies on the accumulation rate of an overlying section. The sections were run as 24.5 cm because the rapid changes in sedimentation found in the core is best represented in the model by breaking it up into smaller sub-units. The left panel of iterations shows a reliable run because the Log of Objectives did not show a systematic drift with the increasing iterations.

$^{87}Sr/^{86}Sr$ and $^{143}Nd/^{144}Nd$ Chemistry

Sediment from core LK12_22, soil, and surface samples from the Ginosar Valley were analyzed for $^{87}Sr/^{86}Sr$ and $^{143}Nd/^{144}Nd$ (Table 3.2; Figs 3.6, 3.7). For the most part, the $^{87}Sr/^{86}Sr$ ratios for the carbonate fraction of the core sediment were uniform with an average value of 0.70767± 0.000644 (1σ).

The $^{87}Sr/^{86}Sr$ ratios and ε_{Nd} values of core LK12_22 samples, averaging 0.70871± 0.001354 (1σ) and -4.2± 0.9 (1σ) respectively, of carbonate-free sediment is variable. In Unit A, the $^{87}Sr/^{86}Sr$ ratios gradually decrease while the ε_{Nd} values increase from the bottom upward until 127 cm and decreases from 127 cm to 123 cm. Units C and D contain the highest $^{87}Sr/^{86}Sr$ ratios whereas ε_{Nd} values are consistently lower than values in Units A and B, ranging from -5.3 to -4.5. $^{87}Sr/^{86}Sr$ ratios and ε_{Nd} values for Units E and F are fairly constant except for a slight increase in both ε_{Nd} and $^{87}Sr/^{86}Sr$ from 25-12 cm.

The $^{87}Sr/^{86}Sr$ ratios and ε_{Nd} values for sediment from the Jordan River channel have $^{87}Sr/^{86}Sr$ ratios generally lower than the core sediment. One sample yielded a ratio of 0.70806, two others are ~0.70494, and one in between with a ratio of 0.70652. The ε_{Nd} values range much more than the core sediment going from -6.6 to -1.5.

Lake surface sediment $^{87}Sr/^{86}Sr$ ratio range (0.70840 to 0.70451) is similar to the Jordan River channel samples and does not go above 0.7085. The ε_{Nd} results produced the widest range of values from -10.1 to -0.2.

Of the ten soil samples analyzed from the East Galilee region, most have carbonate-free $^{87}Sr/^{86}Sr$ ratios that range higher (up to 0.71241) and ε_{Nd} values a little lower than those of core LK12_22. One exception is the sample from a basalt quarry in the Amud catchment (Huk 2) with a $^{87}Sr/^{86}Sr$ ratio of 0.70355 and an ε_{Nd} value of 2.7.

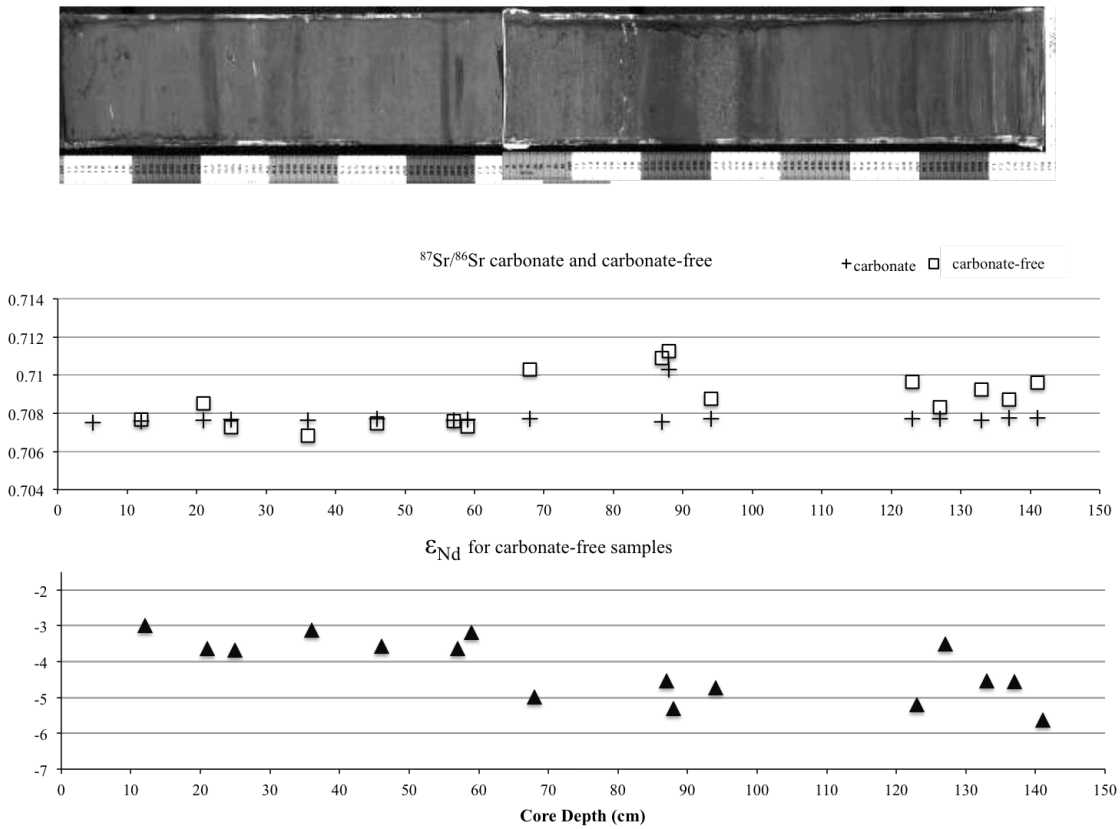

Figure 3.6. $^{87}Sr/^{86}Sr$ and ε_{Nd} results to scale with core image.

Table 3.2.
$^{87}Sr/^{86}Sr$ ratios and ε_{Nd} values for LK12_22 sediment, lake surface, Jordan River and delta, and soil samples.

Sample ID	Core Depth (cm)	Carbonate Fraction		Carbonate-free fraction		
		$^{87}Sr/^{86}Sr$	Sr concentration (ppm)	$^{87}Sr/^{86}Sr$	ε_{Nd}	Sr concentration (ppm)
Core	5.0	0.70751	21.10	NA*	NA*	NA*
Core	12.0	0.70760	26.68	0.70767	-3.0	3.14
Core	21.0	0.70764	12.14	0.70851	-3.6	2.46
Core	25.0	0.70768	15.21	0.70726	-3.7	4.67
Core	36.0	0.70765	19.35	0.70683	-3.1	4.81
Core	46.0	0.70773	19.10	0.70748	-3.6	5.15
Core	57.0	0.70764	21.24	0.70760	-3.6	5.76
Core	59.0	0.70766	23.50	0.70730	-3.2	5.47
Core	68.0	0.70772	22.34	0.71028	-5.0	3.23
Core	87.0	0.70756	10.31	0.71092	-4.5	1.71
Core	88.0	0.71031	7.32	0.71127	-5.3	1.95
Core	94.0	0.70773	4.85	0.70875	-4.7	6.35
Core	123.0	0.70771	15.73	0.70964	-5.2	4.20
Core	127.0	0.70772	14.90	0.70830	-3.5	6.80
Core	133.0	0.70765	16.22	0.70926	-4.5	3.41
Core	137.0	0.70774	20.92	0.70873	-4.6	3.85
Core	141.0	0.70774	18.50	0.70961	-5.6	2.30
LK1	-	0.70750	-	0.70451	-4.7	-
LK7	-	0.70760	-	0.70621	-4.8	-
LK9	-	0.70762	-	0.70708	-10.1	-
LK10	-	0.70763	-	0.70758	-2.7	-
LK12	-	0.70763	-	0.70741	-8.3	-
LK15	-	0.70725	-	0.70742	-10.0	-
LK17	-	0.70763	-	0.70740	-8.8	-
LK41	-	0.70763	-	0.70709	-3.2	-
LK46	-	0.70763	-	0.70781	-0.2	-
LK105	-	0.70773	-	0.70798	-11.2	-
LK122	-	0.70789	-	0.70868	-3.5	-
LK125	-	0.70754	-	0.70884	-1.5	-
LK126	-	0.70725	-	0.70901	-6.6	-
LK159	-	0.70781	-	0.70764	-5.6	-
LK161	-	0.70779	-	0.70840	-5.6	-
Rvd 1	-	-	2.91	0.71193	-5.6	71.01
Rvd 2	-	-	1.76	0.71241	-5.1	66.29
Rvd 3	-	-	4.89	0.71135	-6.1	83.76
Rvd 4	-	-	6.20	0.71116	-5.5	77.67
Amud 1	-	-	10.64	0.70787	-4.9	152.57
Amud 2	-	-	10.04	0.70870	-6.1	188.01
Huk 1	-	-	7.78	0.70916	-6.0	110.37

Sample ID	Core Depth (cm)	Carbonate Fraction		Carbonate-free fraction		
		$^{87}Sr/^{86}Sr$	Sr concentration (ppm)	$^{87}Sr/^{86}Sr$	ε_{Nd}	Sr concentration (ppm)
Huk 2	-	-	3.40	0.70355	2.7	365.67
Khl	-	-	5.15	0.71171	-7.6	75.20
Haz	-	-	1.91	0.71283	-5.4	71.31

*Sample lost

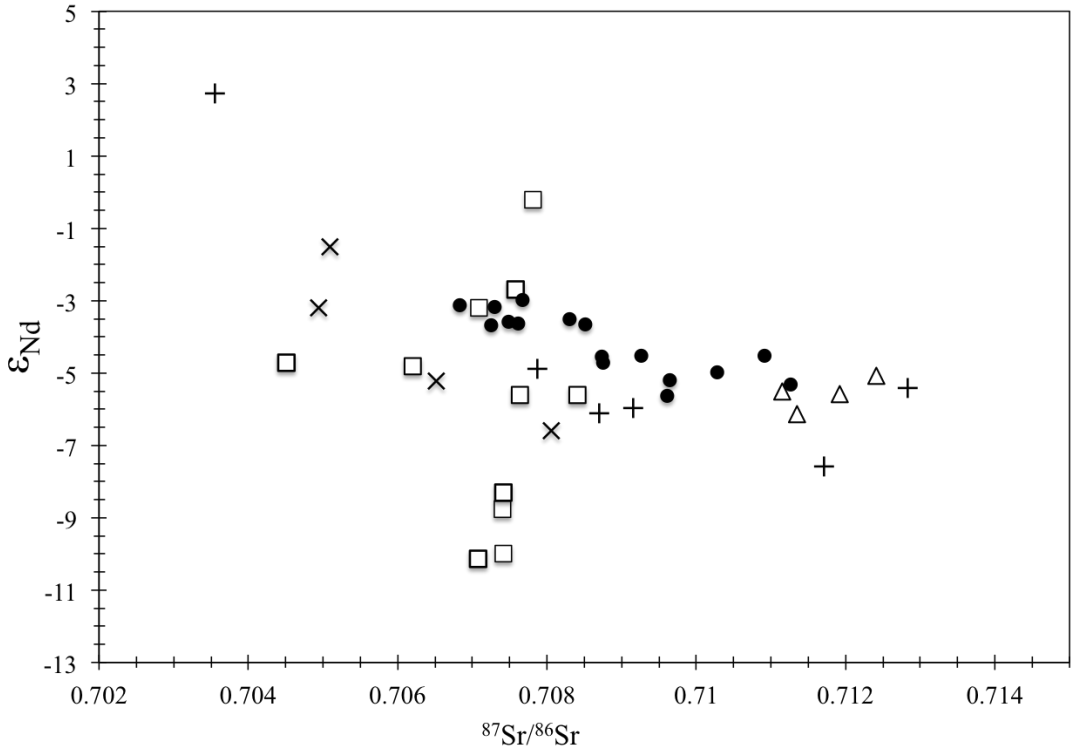

Figure 3.7. Summary plot of the core, soil, and surface sediment samples' $^{87}Sr/^{86}Sr$ ratios and ε_{Nd} values. Core samples = •, lake surface-sediment = □, soils of the Amud catchment = +, soils of the Tsalmon catchment = Δ, and samples from the Jordan River catchment= X.

Chapter 4. Discussion

The ~4000-year history of rainfall and sediment transport from the East Galilee region to the lake was determined by focusing on the grain size of sediments, presence of foraminifer fossils, chronology, and $^{87}Sr/^{86}Sr$ ratios and ε_{Nd} values of the lake surface-sediments and soil samples collected from the Amud and Tsalmon catchments. We identified a number of events based on these parameters and will discuss them here.

The events we observed were (1) the lake level decrease by ~3260 cal BP[1] (110 cm); (2) periods of rapid deposition we interpreted as floods; and (3) a section with missing sediment and an age reversal, which we interpreted as a slope failure in the lake. The floods came from rain events over the East Galilee Mountains while the slope failure may have been the result of a seismic event. The Sea of Galilee's connection to increasing human population and urbanization of the East Galilee and along the western shore of the Sea of Galilee beginning in the Byzantine Period provides a way to support our conclusions based on LK12_22.

The first discovery during the initial core description was a ~20 cm long laminated segment that stood out from the rest of the core. The presence of laminations in lake sediments is likely the result of bottom waters undisturbed from waves and bioturbation due to anoxic conditions. Laminations on a similar scale are not found in any other part of the core, which indicates that this time period was different from more recent lake conditions that did not preserve laminations.

[1] All calendar ages are from Calib 7.1 using IntCal13 calibration curve

The westerly winds off the Mediterranean Sea create windwaves from April through September that cause a counterclockwise gyre to form in the northern 3/4 of the Sea of Galilee. The average wave base of the Sea of Galilee is 10 m, which is also the depth limit of the bottom current transport caused by the gyre (Pan et al., 2002). The parts of the lake with ≤10 m water depth experience regular resuspension of sediment and laminations are not preserved, including most of our core taken from a modern water depth of 10 m (Serruya 1978; Imberger & Marti, 2014). Although we cannot say where the resuspended sediment ultimately settles, the near constant resuspension of sediment, which results in loss of lamination, will provide a lake depth indicator over the time represented in the core.

Deposition of laminated sediment began before ~4000 cal BP (Unit A) with a gradual disappearance of laminations fading into massive sediments (Unit B). Deposition of laminated sediment ceased by ~3260 ±60 cal BP (112.5-111.0 cm) and continued to the top of the Unit D at ~2230 ±100 cal BP (102 cm). This indicates that the lake depth at the core site decreased to ~10 m or less by ~3260 ±60 cal BP (112.5-111.0 cm) allowing the windwaves to resuspend sediment after this time. In addition to the presence of laminations, grain size analysis of the sediments showed that, in general, they contain higher percentages clay and fine silt-sized sediments compared to the rest of the core. This supports the interpretation that the laminated sediments were deposited during a period of higher lake level when the core site was ≥10 m of water.

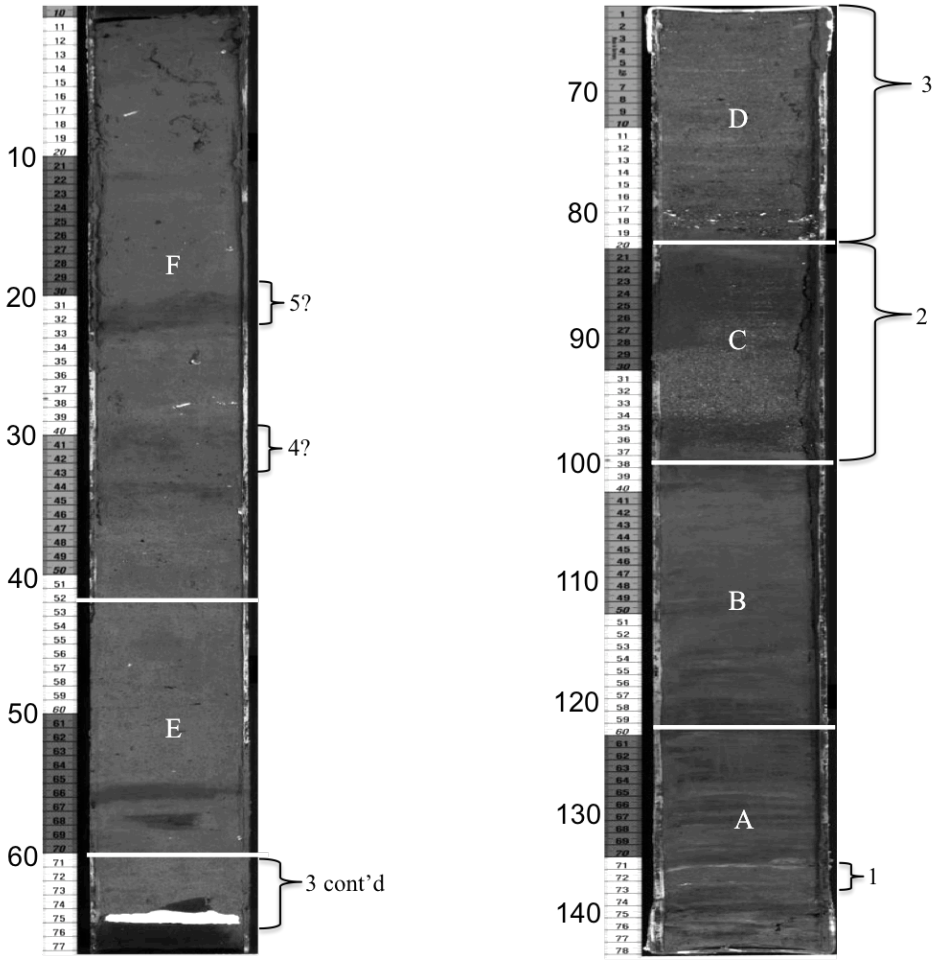

Figure 4.1. Core LK12_22 with flood deposits shown with numbered brackets. Floods 4 and 5 are marked with question marks because they do not share the same characteristics used to identify floods 1-3.

During the initial core description, two adjacent sediment packages from Units C and D stood out as possible turbidites. Continuous grain size analysis of each package showed the average grain size fined up core and the base of each package had a higher percentage of sand sized sediment, which is consistent with a turbidite or flood deposit. Three additional possible flood or turbidite deposits were inferred on the basis of their visual similarities, grain size, presence of fossil foraminifers washed in from the catchment, and broken shells of mollusks living in the lake. Figure 4.1 shows where flood deposits were

found and are numbered in chronological order. These numbers will be used for the remainder of the discussion when identifying specific deposits.

Another indication of a turbidite deposit is the presence of whole and broken shells, including *Melanopsis*, at the base of the flood packages. Their presence is not included in the grain size results because carbonates are dissolved during pretreatment and all material >2 mm is removed before pretreatment. The species of small broken shells were not identified, but *Melanopsis* are frequently found in shallow water in the Sea of Galilee and in the streams and springs feeding the lake (Serruya 1978). *Melanopsis* were likely to have been living in near-shore areas as they are today, transported after death and broken up by wave action and finally deposited as part of the turbidite. The shell-rich sediment must have been washed to deeper water depths during floods from the Amud or Tsalmon streams because the shells were likely originally concentrated as lag deposits at shallower depths. If the bottom currents were consistently transporting shell material, shells would be more evenly distributed throughout the sediment core rather than in distinct layers.

There are also foraminifer fossils of Late Cretaceous to Eocene age found throughout both Floods 2 and 3, but are more abundant in Flood 2. These fossils are derived from the limestones and dolostones found in the Amud and Tsalmon catchments. As the carbonate rock weather, the foraminifers are freed and are incorporated into the watershed and deposited into the lake with other sediment and water (Lev, et al., 2014). The inferred flood deposits contain sand-rich sediment mixed with shells and their debris at the base, so they did not travel far from where they were originally deposited during

flood events (Laronne & Shlomi, 2007). In general, sediment's coarseness correlates to the distance traveled because the water carrying the sediment drops the largest material first (Abeyta & Paola, 2015).

Another distinctive feature of each flood package aside from upward fining trend is their distinct color compared to the rest of core LK12_22. The sediment in Flood 2 is brick red in color and Flood 3 is a very dull gray. The sediment in the rest of the core is a variation of taupe, reddish brown, or grayish brown but not simply gray like Flood 3. There are other 1-cm thick dark red layers like Flood 2 found at 55 and 22 cm that were also considered potential flood deposits for further geochemical analysis. The distinct colors of the flood packages provide a visual clue that the floods came from separate watersheds rather than from the broader East Galilee.

The colors of the turbidites led to the idea of trying to identify the sources of core sediment and to see if we can discern whether the floods were local (e.g. one watershed) or regional (e.g. East Galilee) in origin. The $^{87}Sr/^{86}Sr$ ratios and ε_{Nd} values from the core sediment, lake surface sediments, and soils from the Amud and Tsalmon catchments were used to trace the core sediment to their likely sources including the Jordan River, Amud, and Tsalmon watersheds. Overall, the $^{87}Sr/^{86}Sr$ ratios from the carbonate fraction of sediment are a reflection of the Late Cretaceous to Eocene (DePaolo & Ingram, 1985) local carbonate rocks in the region (Table 3.2), which provided solutes to the lake from which endogenic calcite precipitated. There is one sample with a ratio of 0.71031 from Flood 2 at 88 cm that is not included in the average because it is outside the range of measured $^{87}Sr/^{86}Sr$ ratios found in Late Cretaceous to Eocene marine carbonate samples

from DSDP cores and a variety of fossil mollusks and foraminifer (DePaolo & Ingram, 1985; Ehrlich, et al., 2001).

The carbonate-free fraction of the core analyzed for $^{87}Sr/^{86}Sr$ ratios and ε_{Nd} values from Flood 2 (101-83 cm), the dark red flood deposit, are similar to the values from the Amud catchment soils (cross symbols in Figure 4.2). Similarly, the $^{87}Sr/^{86}Sr$ ratios and ε_{Nd} values from Flood 3 (83-60 cm) are similar to the soils in the Tsalmon catchment (open triangle symbols in Figure 4.2). The similarity of $^{87}Sr/^{86}Sr$ ratios and ε_{Nd} values between the turbidites and samples from each catchment provides geochemical evidence of the flood's source. The isotopic values also revealed another flood deposit (Flood 1) from the Amud catchment in the core at 137 cm depth because its $^{87}Sr/^{86}Sr$ ratios and ε_{Nd} values fell very close to the Amud catchment values. The sediment at 137 cm is a sandy layer about 1-cm thick within the laminated portion of the core. Flood 1 originally was not noticed because it is not nearly as thick, fining upward grain size change is not visually evident, and there are fewer broken shells at the base. Samples for grain size analysis were not taken contiguously, so there are no analyses between 137 cm and 134 cm, but the percentage of sand sized grains decreases by half from a sample at 137 cm to another at 134 cm and the percentage of clays doubles over the same interval.

The carbonate-free core sediment not associated with Floods 1-3 tends to have a narrower range of ε_{Nd} values and $^{87}Sr/^{86}Sr$ ratios compared to the turbidites. The ε_{Nd} values range from -3.0 to -3.7 and all but one $^{87}Sr/^{86}Sr$ ratios are ~0.707. Comparison of the upper 59 cm of the core to lake surface-sediment (open square symbols on Figure 4.2) and the Jordan River channel samples (X symbols in Figure 4.2) showed how the two

sample groups intersect with the core sediment. The Jordan River channel samples capture the regular winter rainfall that feeds the Sea of Galilee. Some of the samples from the Jordan catchment have lower $^{87}Sr/^{86}Sr$ ratios (~0.706) that overlap with some of the core values (~0.708). The lake surface-sediment samples not directly deposited by a stream have a broad range of ε_{Nd} values and $^{87}Sr/^{86}Sr$ ratios with some overlap with the Jordan River channel, Amud catchment, and LK12_22 samples. The Jordan River is the main water and sediment source for the Sea of Galilee (Rimmer & Givati, 2014), which is why the surface-sediment samples taken off-shore the Jordan River mouth (e.g. LK7) intersect with the Jordan River channel samples. The ε_{Nd} values and $^{87}Sr/^{86}Sr$ ratios of non-turbidite core sediment are roughly in-between the Jordan River channel and surface-sediment samples. This suggests that the sediment in the upper 59 cm of LK12_22 is likely comprised of the Jordan River sediment and Aeolian material falling directly into the lake.

The Levant is strongly affected by the Cyprus Low pressure system, which brings winter rain and dust from the Saharan Shield, Arabian-Nubian Shield, and Ethiopian Highlands (Palchan et al., 2013). All carbonate-free sediment studied for this project yielded isotopic results that fall in a field in-between the known $^{87}Sr/^{86}Sr$ ratios and ε_{Nd} values of dust sources (Figure 4.2). The Amud and Tsalmon catchment soils appear to have some influence from these sources based on higher $^{87}Sr/^{86}Sr$ ratios than the Jordan River and open lake surface-sediment samples.

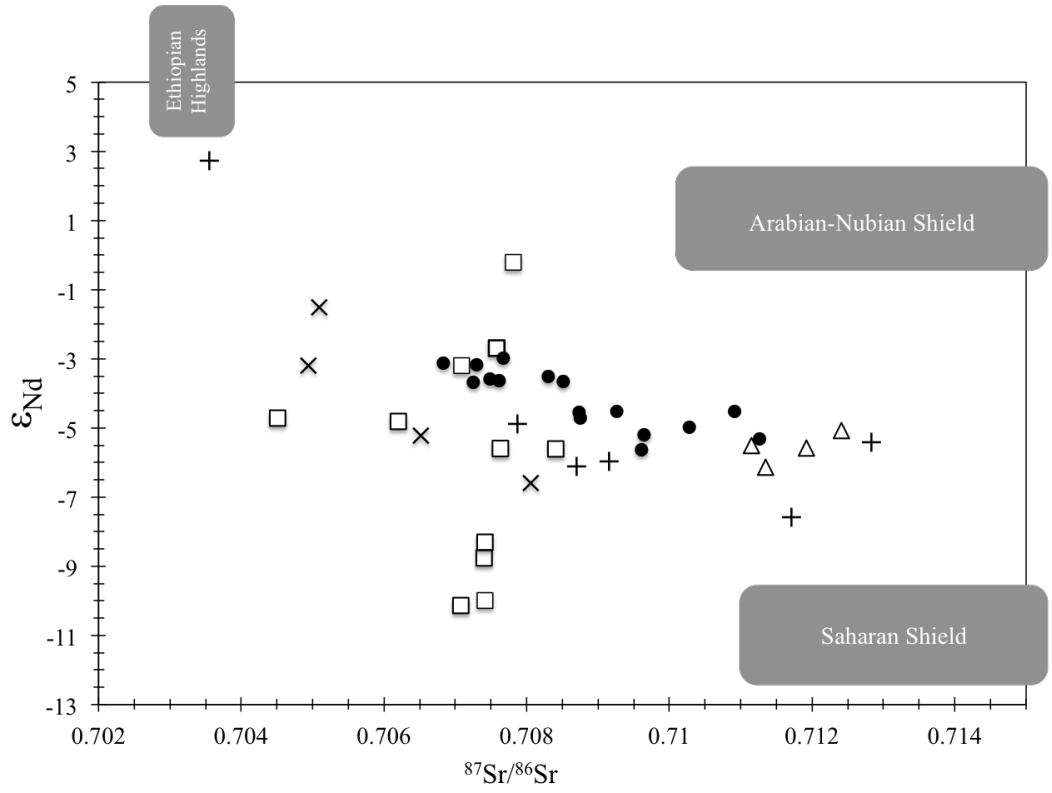

Figure 4.2. Carbonate-free $^{87}Sr/^{86}Sr$ ratios and ε_{Nd} values of the lake sediment soil samples and dust from the Ethiopian Highlands, Saharan Shield and Arabian-Nubian Shield.
Core samples = •, surface-sediment from lake = □, soils of the Amud catchment = +, soils of the Tsalmon catchment = Δ, and samples from the Jordan River channel= X.

Possible flood events 4 and 5 were identified on the basis of grain size, soft sediment deformation, and foraminifer fossils. However, $^{87}Sr/^{86}Sr$ ratios and ε_{Nd} values of sample from 36 cm depth in the core (Flood 4) and 21 cm depth (Flood 5) are not like those seen for Flood 2 and 3 deposits, which were easily traced to soil samples from the Amud or Tsalmon catchments. Flood 4 and 5 events are labeled with question marks on Figure 4.1 because of these mismatches. The soft sediment deformation is the flame structure (37-35 cm), which is generally caused by the sudden deposition of denser sediment onto less dense sediment, such as the water-rich sediment found near the sediment-water interface.

Some soil samples taken from the Amud and Tsalmon catchments have ε_{Nd} values between the dust from Saharan Shield and the Arabian-Nubian Shield and $^{87}Sr/^{86}Sr$ ratios between these two shields and dust from the Ethiopian Highlands (Figure 4.2). Floods 2 and 3 sediment gave $^{87}Sr/^{86}Sr$ ratios and ε_{Nd} values that showed contribution of Aeolian dust from all three source regions mixed with local regolith material. Floods 4 and 5 were smaller events, and based on their fine grain size, were perhaps nearly entirely comprised of dust with no local regolith material.

The chronology of core LK12_22 presented unexpected evidence for lost sediment possibly caused by a slope failure event. The sudden decrease in the apparent sedimentation rate between 43 cm (~530 cal yrs BP) and 52 cm (~1480 cal yrs BP) and an age reversal at 56 cm (~1220 cal yrs BP) launched further modeling and calibration comparison using Bacon and Calib 7.1 to see if we could narrow down the timing of the possible slope failure. All Bacon age-depth models rejected 1480 cal yrs BP at 52 cm and chose calibrated dates that retained the sediment's chronological order. Also, possibly because of the young age of the core (~4000 cal yrs BP at the base), Bacon 2.2 did not allow us to independently model age-depth relation for one segment above the slope failure and another segment below the Flood 2. Because of these problems with Bacon 2.2, instead of creating an age-depth model, we use Calib 7.1 calendar ages derived for each ^{14}C age (see Appendix).

The apparent sedimentation rate calculated for the uppermost ~43 cm is ~0.07 cm/yr which decreases to ~0.02 cm/yr for 52-43 cm. If the higher sedimentation rate applied to 1480 cal yrs BP (52.5 cm), there should be a total of 110 cm of sediment rather

than the observed 52 cm, or an additional 50-60 cm of sediment between 52 and 43 cm. This translates to about 700 to 850 years of missing sediment. The likely reason for the apparently missing sediment and a younger age of ~1220 cal yrs BP at 56 cm is a slope failure because a sudden loss of lake sediment will appear as missing time (Francke, et al. 2013, Bonnecaze, et al., 1993). The failure of part of the delta foreset could easily have disrupted the chronological order of the accumulated sediment.

In addition to chronological and sedimentation rate argument, an isolated clay-rich layer at 56 cm and an angular bleb of similar fine-grained sediment at 58 cm can be offered as further pieces of evidence of the slope failure. The angular bleb of clayey sediment could have been ripped up during the slope failure event from a fine-grained sediment layer that had been deposited upslope from the core site and redeposited with the more typical silt sized sediment. The isolated layer of clay-sized sediment is also dark brownish red and is thinner on one side. It could be that this layer is another type or "rip up clast" like the angular bleb, but that it was a not broken up into smaller pieces during transport. The slope-failure event removed lake sediment from the core site and transported the older sediment from upslope area to the core site. The slope failure may have been due to (1) gradual sediment and water input from the East Galilee, (2) large surge of water and sediment draining from the Amud or Tsalmon, or (3) a seismic event.

(1) Gradual input from the Amud and/or Tsalmon streams could have caused the slope failure. Such events are not necessarily triggered by sudden increases in sediment delivery because sediment is generally spread out evenly over the delta as it enters the lake rather than remain in one channel, but the Amud and Tsalmon remain the most direct

source of water and sediment to the core site. The sediment-laden water going into the lake could cause unstable foreset to be transported to a deeper part of the lake when the angle between the foreset and toeset of the delta reaches a critical value (Abeyta & Paola, 2015, Figure 3). The gradual increase of sediment creates a convex foreset that eventually becomes unstable and results in loss of foreset sediment and headward erosion (Abeyta & Paola, 2015).

(2) Sudden input of water and sediment from streams draining the East Galilee could have caused a flood triggering the slope failure. Rainfall events on the East Galilee produce turbid input into the lake, especially after prolonged dry periods when more Aeolian dust has accumulated in the catchments (Reichman, et al., 2014). Flash flood events are common in the Dead Sea Rift Valley due to the infrequent rain in the arid climate (Laronne & Shlomi, 2007). When it does rain, the dust and other loose material resting on the landscape are washed into the stream channels and are quickly transported into the lake as a large plume. A flood event could have brought sediment-laden water that overloaded the foreset and triggered the slope failure event.

(3) The last cause we consider is a magnitude 7 earthquake that occurred on 18 January, 746 CE (1204 cal BP) near 32°N and 35.5°E (National Geophysical Center). This earthquake is known as the Sabbatical Earthquake and caused near complete destruction of Byzantine cities of Tiberias (6 km south of Ginosar), Jericho (114 km south of Ginosar), and Capernaum (5 km north of Ginosar), seiche in the Dead Sea, and tsunami in the Mediterranean Sea (Menahem, 1991; Marco, et al. 2003). It must have also strongly affected the Ginosar area and could have caused the slope failure. East Galilee

area has abundant faults related to the major Dead Sea Transform, which in historical times have caused landslides (GSI Geologic Map of Israel). The charcoal sample LK6 at 56 cm gives Calib 7.1 age of 1220 ±70 cal yrs BP. The features such as possible rip-up clasts, soft sediment deformation, and older sediment age (1480 ±45 cal yrs BP at 43 cm) all occur above 56cm, consistent with earthquake-triggered slope failure. High-resolution studies of other cores taken from the Sea of Galilee may show a similar disruption of sedimentary structure for the same time.

We looked for findings from archaeological and palynological studies to compare with the flood and slope failure events recorded in LK12_22 to see if these events have any relation to climate and human occupation of the East Galilee. Palynological studies were conducted on Lake Kinneret cores KIN4D (also known as KIND-4 or KIN4; 32.747483, 35.58284; Baruch, 1986) and Ki-10 (32°49'13.8" N, 35°35'19.7" E; Langutt et al., 2013; Schiebel, 2013).

Langutt et al. (2013) correlated the period of increased relative abundance of tree pollens, especially of olives, and the appearance of walnut and common vine grapes to the Iron Age 1 (1200-1000 BCE). However, the period showing a similar increase in olive pollen and appearance of walnut studied by Baruch (1986) and interpreted as the same event by Langutt et al. (2013) is dated to ~2200-1000 cal yrs BP (250-950 CE), much younger than the Iron Age (1200-586 BCE). The calibrated age we obtained for a charcoal sample from 103.5-102.0 cm near the top of Unit B is 2235 ±100 cal BP (285 BCE). So, while the Floods 2 and 3 do not seem related to increased population and olive cultivation during the Iron Age I (Cheson, 1999; Münger et al., 2011), they may

still be related to increased soil erosion connected to deforestation and olive cultivation during late Roman and Byzantine periods when there were large population centers along the western shore of the Sea of Galilee.

Chapter 5. Summary and Future Work

Core LK12_22 captured the Sea of Galilee undergoing a gradual water level decrease, several floods from the Amud and Tsalmon, and at least one slope failure event over the past ~4000 yrs. Due to the relatively infrequent precipitation in the East Galilee, the sediment accumulation was highly sensitive to changes in sediment availability, which created a variety of deposits over a relatively short period of time.

1. Unit A of the core was deposited during a period of higher lake level, which preserved laminations. The laminations are mostly silt-sized sediments with one small flood deposit (Flood 1) with $^{87}Sr/^{86}Sr$ ratio and ε_{Nd} value of carbonate-free fraction similar to the soils from the Amud catchment and has a base with broken shells.
2. The core site accumulated sediment from the East Galilee as large isolated depositional events as well as sediment that has carbonate-free fractions with $^{87}Sr/^{86}Sr$ ratios and ε_{Nd} values similar to the Jordan River delta. The range of $^{87}Sr/^{86}Sr$ ratios and ε_{Nd} values of the carbonate-free fractions of the core indicate that they are a mix of Aeolian dust from three sources: the Ethiopian Highlands, Saharan Shield, and Arabian-Nubian Shield. The $^{87}Sr/^{86}Sr$ ratios of carbonate fractions are consistent with $^{87}Sr/^{86}Sr$ of Late Cretaceous to Eocene marine carbonate rocks, which are present in the East Galilee.
3. Floods 1-3 are more isotopically ($^{87}Sr/^{86}Sr$ ratios and ε_{Nd} values) and mineralogically similar to the soil samples from Amud and Tsalmon catchments. The deposits' color may mean that the red sediment from Floods 1 and 2 had a source with Terra Rossa

soils common in the Amud catchment and Flood 3 with brown/tan color came from a Rendzina soil found in the Tsalmon catchment.

4. The age reversal in Unit E is most likely the result of a slope failure of Amud/Tsalmon delta. The probable age of this event estimated from the age of the intact sediment near the bottom of Unit E ties the slope failure to the magnitude 7 earthquake (32° N, 35.5° E) that occurred in 746 CE.
5. Massive Floods 2 and 3 may have occurred during the Byzantine Period coincident with the timing of increased relative abundance of olive pollen in core KIND-4 (Baruch, 1986). These floods probably occurred well before the 746 CE earthquake because we have a date of 728 CE for charcoal from near the bottom of Unit E, 4 cm above the Flood deposits (Units C and D).

Future Work

Additional dating of core LK 12_22 to narrow down the possible age of the slope failure occurrence (Unit E) will help strengthen (or weaken) the 746 CE earthquake as its trigger. Study of other cores collected during January of 2012 to see if they also contain records of flood or slope failure will provide a better map of the sediment distribution in the Sea of Galilee and how far into the lake basin sediment from Amud and Tsalmon is delivered. Studies of these other cores should include chronology, XRD/smear slide mineralogy, grain size analysis, and $^{87}Sr/^{86}Sr$ and $^{143}Nd/^{144}Nd$ isotope ratio analyses of selected samples. Longer cores from near the core LK 12_22 site may allow us to reconstruct older flood events from Amud and Tsalmon. Because of long human

occupation of the East Galilee it would be interesting to see if flood events can be correlated to the periods of higher population possibly indicating wetter climate of the region.

Bibliography

Abeyta, A. & Paola, C., 2015. Transport dynamics of mass failures of weakly cohesive clinoform foresets. Sedimentology, 62:303-313.

Alpert P., Cohen, A., and Neumann, J., 1982. A model simulation of the summer circulation from the eastern Mediterranean past Lake Kinneret in the Jordan Valley. Monthly Weather Review, 110:994-1006.

Avissar, R. and Pan, H., 2000. Simulations of the summer hydrometeorological processes of Lake Kinneret. Journal of Hydrometeorology, 1:95-109.

Bar-Yosef, O (1998) The Natufian culture in the Levant, threshold to the origins of agriculture. *Evolutionary Anthropology Issues News and Reviews*, 6: 159–177.

Baruch, U., 1986. The Late Holocene vegetational history of Lake Kinneret (Sea of Galilee), Israel. Paléorient, 12: 37-48.

Ben-Avraham, Z., Rosenthal, M., Tibor, G., Navon, H., Wust-Bloch, H., Hofstetter, R., and Rybakov, M., 2014. Chapter 2. Structure and Tectonic Development of the Kinneret Basin. In Zohary, T., Sukemik, A., Berman, T., and Nishri, A. (eds) *Lake Kinneret, Ecology and Management*. Springer. New York, pp 19-38.

Berman, T., Zohary, T., Nishri, A., and Sukenik, A., 2014. Chapter 1. General Background, In Zohary, T., Sukemik, A., Berman, T., and Nishri, A. (eds*) Lake Kinneret, Ecology and Management*. Springer. New York, pp. 1-15.

Blaauw, M. & J. A. Christen, 2011. Flexible paleoclimate age-depth models using an autoregressive gamma process. Bayesian Analysis, 6: 457-474 doi: 10.1214/11-BA618.

Bonnecaze, R.T, H. E. Huppert, and J. R. Lister, 1993. "Particle-driven gravity currents," Journal of Fluid Mechanics, 250: 339-369.

Cheson, M. 1999. Libraries of the Dead: Early Bronze Age Charnel Houses and Social Identity at Urban Bab edh-Dhra', Jordan. Journal of Anthropological Archaeology, 18: 137–164

DePaolo, D. & Ingram, B, 1985. High-Resolution Stratigraphy with Strontium Isotopes. Science, 227: 938-941.

Ehrlich, S., Gavrieli, I., Dor, L.-B., Halicz, L., 2001. Direct high-precision measurements of the $^{87}Sr/^{86}Sr$ isotope ratio in natural water, carbonates and related materials by multiple collector inductively coupled plasma mass spectrometry (MC-ICP-MS). Journal of Analytical Atomic Spectrometry 16: 1389–1392

Enzel, Y., Bookman (Ken Tor), R., Sharon, D., Gvirtzman, H., Dayan, U., Ziv, B., and Stein, M., 2003. Late Holocene climates of Near East deduced from Dead Sea level variations and modern regional winter rainfall. Quaternary research, 60:263-273.

Finkelstein I. 1995. The great transformation: the "conquest" of the highlands frontiers and the rise of the territorial states. In: Levy, T. E., (ed), *The Archaeology of Society in the Holy Land*. London: Leicester University Press. Pp. 349–65

Flexer, A., Kronfeld, J., Rosenthal, E., Ben-Avraham, Z., Artsztein, P.P., and Davidson, L., 2000, A Neogene salt body as the primary source of salinity in Lake Kinneret. Archiv für Hydrobiologie, Advances in Limnology, 55:69-85.

Francke, A., V. Wennrich, M. Sauerbrey, O. Juschus, M. Melles, J. Brigham-Grette Multivariate statistic and time series analysis of grain-size data in quaternary sediments of Lake El'gygytgyn, NE Russia. Climate of the Past, 9: 2459–2470

Ganor, E., Deutsch, Y., and Foner, H. A., 2000. Mineralogical composition and sources of airborne settling particles on Lake Kinneret (the Sea of Galilee), Israel. Water, Air, and Soil Pollution, 118:245-262.

Garcia-Veigas, J., Rosell, L., Zak, I., Playa, E., Ayora, C., and Starisky, A., 2009. Evidence of potash salt formation in the Pliocene Sedom Lagoon (Dead Sea Rift, Israel). Chemical Geology, 265:499-511.

Goldreich, Y., 1995. Temporal variations of rainfall in Israel. Climate Research, 5:167-179.

Gophen, M. 2011. Hula Valley Wetlands (Israel). https://www.iisd.org/pdf/2011/hula.pdf

Gross, A., Nishri, A., Angert, A., 2013. Use of phosphate oxygen isotopes for identifying atmospheric-P sources: a case study at Lake Kinneret. Environmental Science & Technology, 47:2721-2727.

Gvirtzmann, H., Garven, G., and Gvirtzman, G., 1997. Hydrological modeling of the saline hot springs at the Sea of Galilee, Israel. Water Resources Research, 33:913-926.

Haliva-Cohen, A., Stein, M., Goldstein, S. L., Sandler, A., and Starinsky, A., 2012. Sources and transport routes of fine detritus to the Late Quaternary Dead Sea Basin. Quaternary Science Reviews, 49:1-16.

Imberger, J., and Marti, C. L., 2014. Chapter 9. The Seasonal Hydrodynamic Habitat. In Zohary, T., Sukemik, A., Berman, T., and Nishri, A. (eds) *Lake Kinneret, Ecology and Management*. Springer. New York, pp. 133-157.

Koren. N. and Klein, M. 2000. Rate of sedimentation in Lake Kinneret, Israel: spatial and temporal variations. Earth Surface Processes and Landforms, 25, 895-904.

Langutt, D., Finkelstein, I., and Litt, T., 2013. Climate and the Late Bronze collapse: new evidence from the southern Levant. Tel Aviv: Journal of the Institute of Archaeology of Tel Aviv University, 40:149-175.

Langutt, D., Finkelstein, I., Litt, T., Neumann, F. H., and Stein, M., 2015. Vegetation and climate changes during the Bronze and Iron Ages (~3600-600 BCE) in the southern Levant based on palynological records. Radiocarbon, 57:217-235.

Laronne, J. & Shlomi, Y., 2007. Depositional character and preservation potential of coarse grained sediments deposited by flood events in hyper-arid braded channels in the Rift Valley, Arava, Israel. Sedimentary Geology, 195: 21-37.

Lev, L., A. Almogi-Labin, S. Mischke, E. Ito, Z. Ben-Avraham, M. Stein, 2013. Paleohydrology of Lake Kinneret during the Heinrich event H2. Palaeogeography. Palaeoclimatology. Palaeoecology, 396: 183–193

Lugmair, G., Scheinin. N., Marti, K., 1975. Sm-Nd age and history of Apollo 17 basalt 75075-evidence for early differentiation of the lunar exterior. Lunar and Planetary Science Conference Proceedings, pp. 1419-1429.

Marco, S., Hartal, M., Hazan, N., Lev, L., Stein, M. 2003. Archaeology, history, and geology of the A.D. 749 earthquake, Dead Sea transform. Geology, 31:665-668

Menahem, AB. 1991. Four thousand years of seismicity along the Dead Sea Rift. Journal of Geophysical Research, 96:196-20, 216.

Münger, S., Zangenberg, J., Pakkala, J. 2011. Kinneret- An Urban Center at the Crossroads: Excavations on Iron 1B Tel Kinrot at the Lake of Galilee. Near East Archaeology, 74:68-90.

National Geophysical Data Center / World Data Service (NGDC/WDS): Significant Earthquake Database. National Geophysical Data Center, NOAA. doi: 10.7289/V5TD9V7K

Nishri, A., Stiller, M., Rimmer, A., Geifman, Y., and Krom, M., 1999. Lake Kinneret (the Sea of Galilee): the effects of diversion of external salinity sources and probable chemical composition of the internal salinity sources. Chemical Geology, 158:37-52.

Palchan, D., M. Stein, A. Almogi-Labin, Y. Erel, S.L. Goldstein, 2013. Dust transport and synoptic conditions over the Sahara-Arabia deserts during the MIS6/5 and 2/1 transitions from grain-size, chemical and isotopic properties of Red Sea cores. Earth and Planetary Science Letters, 382: 125–139

Pan, H., Avissar, R., and Haidvogel, D. B., 2002. Summer circulation and temperature structure of Lake Kinneret. Journal of Physical Oceanography, 32:295-313.

Pennington, W., 1991. Palaeolimnology in the English Lakes - some questions and answers over fifty years. Hydrobiologia, 214: 9-24.

Reichman O., Omer, D. and Markel, D., 2014. Tracing river load in streams discharging Lake Kinneret. The Israel Water Authority Report on Project No. 9588080554.

Reimer, P. J., E. Bard, A. Bayliss, J. W. Beck, P. G. Blackwell, C. Bronk Ramsey, C. E. Buck, H. Cheng, R. L. Edwards, M. Friedrich, P. M. Grootes, T. P. Guilderson, H. Haflidason, I. Hajdas, C. Hatté, T. J. Heaton, A. G. Hogg, K. A. Hughen, K. Kaiser, B. Kromer, S. W. Manning, M. Niu, R. W. Reimer, D. A. Richards, E. M. Scott, J. R. Southon, C. S. M. Turney & J. van der Plicht, 2013. IntCal13 and MARINE13 radiocarbon age calibration curves 0-50000 years cal BP. Radiocarbon 55(4):1869-1887 doi: 10.2458/azu_js_rc.55.16947

Rimmer, A., and Givati, A., 2014. Chapter 7. Hydrology. Zohary, T., Sukemik, A., Berman, T., and Nishri, A. (eds) *Lake Kinneret, Ecology and Management*. Springer. New York, pp. 97-111.

Schiebel, V., 2013. Vegetation and climate history of the southern Levant during the last 30,000 years based on palynological investigation. Unpublished RNDr. thesis. University of Bonn. 104p.

Serruya, C. (ed.) 1978. *Lake Kinneret*. Dr. W. Junk by Publishers, The Hague. 501p.

Shteinman, B., Kamenir, Y., Gophen, M., 1999. Effect of hydrodynamic factors on benthic communities in Lake Kinneret. Hydrobiologia, 408:211-216.

Singer, A., 2007. *The Soils of Israel*. Springer-Verlag, Berlin. 306p.

Singer, A., Gal, M. and Banin, A., 1972. Clay minerals in recent sediments of Lake Kinneret (Tiberias), Israel. Sedimentary Geology, 8:289-308.

Singer, A., Ganor, E., Dultz, S., Fischer, W., 2003. Dust deposition over the Dead Sea. Journal of Arid Environments, 53: 41-59.

Stuiver, M., Reimer, P. J., and Reimer, R. W. 2005. CALIB 5.0. [WWW program and documentation].

Tanaka, T., Togashi, S., Kamioka, H.,Amakawa, H., Kagami, H.,Hamamoto, T., Yuhara, M., Orihashi, Y., Yoneda, S., Shimizu, H., 2000. JNdi-1: a neodymium isotopic reference in consistency with LaJolla neodymium. Chemical Geology, 168: 279–281.

Tsafrir, Y., & Foester, G., 1992. The dating of the earthquake of the sabbatical-year of 749 CE in Palestine. Bulletin of the School of Oriental and African Studies, University of London, 55: 231-235

USGS, El-Naser,H., Nuseibeh, M.F., Assaf, K.K., Kessier, S., Ben-Zui, M., 1998. Overview of Middle East Water Resources: Water Resources of Palestine, Jordanian, and Israeli Interest. USGS, Reston, VA.

Williams, A., Ito, E., Kalanke, J., Mischke, S., Stefanova, I., Stein, M., and Almogi-Labin, A. (in prep.) Late Holocene hydroclimatic and hydrochemical history of the

Sea of Galilee, Israel: ostracode evidence. To be submitted to the Journal of Micropalaeontology.

Appendix

Calib 7.1 results and probability curves

```
LK1
Lab Code
Sample Description
Radiocarbon Age BP    275 +/-   35
Calibration data set: intcal13.14c                # Reimer et al. 2013
  % area enclosed       cal BP age ranges           relative area under
                                                  probability distribution
  68.3 (1 sigma)     cal BP 287 - 320                      0.472
                            378 - 427                      0.528
  95.4 (2 sigma)     cal BP 0 - 2                          0.003
                            153 - 168                      0.048
                            282 - 335                      0.403
                            348 - 458                      0.546
  Median Probability:   362

 References for calibration datasets:
Reimer PJ, Bard E, Bayliss A, Beck JW, Blackwell PG, Bronk Ramsey C, Buck CE
Cheng H, Edwards RL, Friedrich M, Grootes PM, Guilderson TP, Haflidason H,
Hajdas I, HattÃ© C, Heaton TJ, Hogg AG, Hughen KA, Kaiser KF, Kromer B,
Manning SW, Niu M, Reimer RW, Richards DA, Scott EM, Southon JR, Turney CSM,
van der Plicht J.
IntCal13 and MARINE13 radiocarbon age calibration curves 0-50000 years calBP
Radiocarbon 55(4). DOI: 10.2458/azu_js_rc.55.16947

Comments:
* This standard deviation (error) includes a lab error multiplier.
** 1 sigma = square root of (sample std. dev.^2 + curve std. dev.^2)
** 2 sigma = 2 x square root of (sample std. dev.^2 + curve std. dev.^2)
where ^2 = quantity squared.
[ ] = calibrated range impinges on end of calibration data set
0* represents a "negative" age BP
1955* or 1960* denote influence of nuclear testing C-14

NOTE:  Cal ages and ranges are rounded to the nearest year which
       may be too precise in many instances.  Users are advised to
       round results to the nearest 10 yr for samples with standard
       deviation in the radiocarbon age greater than 50 yr.
```

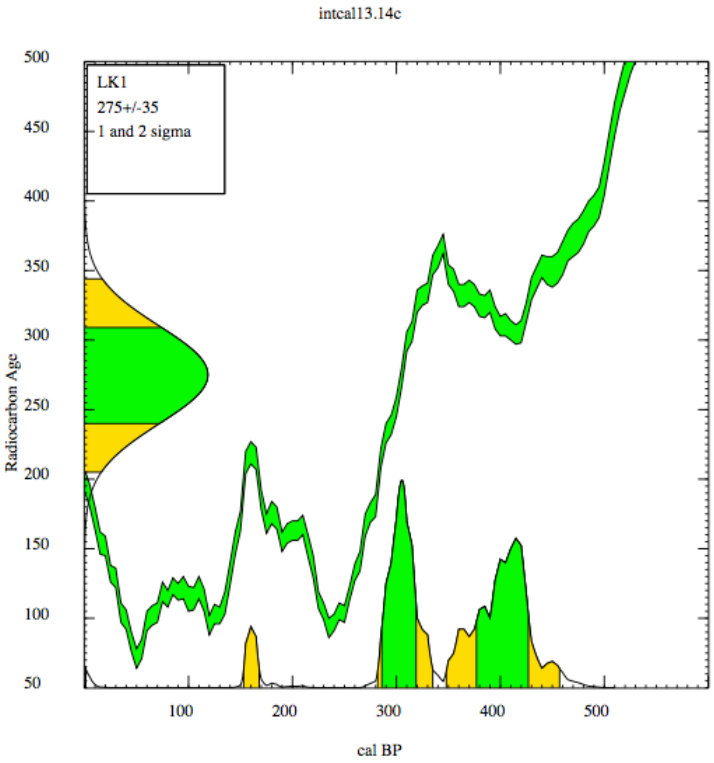

LK2
Lab Code
Sample Description
Radiocarbon Age BP 200 +/- 30
Calibration data set: intcal13.14c # Reimer et al. 2013

% area enclosed	cal BP age ranges	relative area under probability distribution
68.3 (1 sigma)	cal BP 0 - 12	0.167
	148 - 187	0.522
	208 - 211	0.028
	270 - 292	0.283
95.4 (2 sigma)	cal BP 0 - 24	0.161
	141 - 220	0.567
	263 - 303	0.272

Median Probability: 179

References for calibration datasets:

Reimer PJ, Bard E, Bayliss A, Beck JW, Blackwell PG, Bronk Ramsey C, Buck CE Cheng H, Edwards RL, Friedrich M, Grootes PM, Guilderson TP, Haflidason H, Hajdas I, HattÃ© C, Heaton TJ, Hogg AG, Hughen KA, Kaiser KF, Kromer B, Manning SW, Niu M, Reimer RW, Richards DA, Scott EM, Southon JR, Turney CSM, van der Plicht J.
IntCal13 and MARINE13 radiocarbon age calibration curves 0-50000 years calBP
Radiocarbon 55(4). DOI: 10.2458/azu_js_rc.55.16947

Comments:
* This standard deviation (error) includes a lab error multiplier.
** 1 sigma = square root of (sample std. dev.^2 + curve std. dev.^2)
** 2 sigma = 2 x square root of (sample std. dev.^2 + curve std. dev.^2)
where ^2 = quantity squared.
[ ] = calibrated range impinges on end of calibration data set
0* represents a "negative" age BP
1955* or 1960* denote influence of nuclear testing C-14

NOTE: Cal ages and ranges are rounded to the nearest year which may be too precise in many instances. Users are advised to round results to the nearest 10 yr for samples with standard deviation in the radiocarbon age greater than 50 yr.

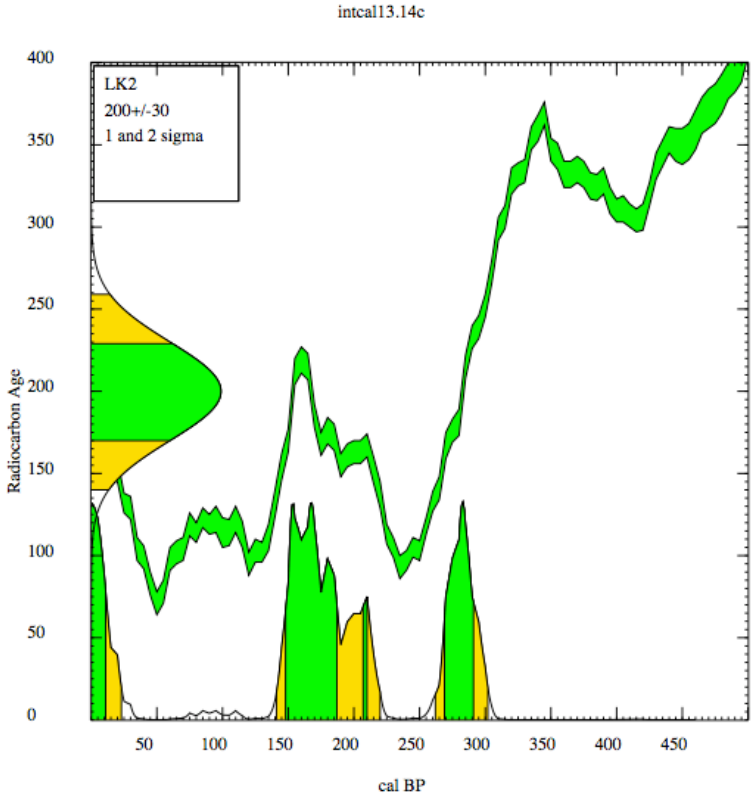

```
LK3
Lab Code
Sample Description
Radiocarbon Age BP     335 +/-   40
Calibration data set: intcal13.14c                # Reimer et al. 2013
  % area enclosed       cal BP age ranges             relative area under
                                                   probability distribution
  68.3 (1 sigma)      cal BP 316 - 340                      0.199
                             347 - 400                      0.457
                             402 - 406                      0.023
                             422 - 460                      0.321
  95.4 (2 sigma)      cal BP 306 - 486                      1.000
  Median Probability:    393

 References for calibration datasets:
Reimer PJ, Bard E, Bayliss A, Beck JW, Blackwell PG, Bronk Ramsey C, Buck CE
Cheng H, Edwards RL, Friedrich M, Grootes PM, Guilderson TP, Haflidason H,
Hajdas I, HattÃ© C, Heaton TJ, Hogg AG, Hughen KA, Kaiser KF, Kromer B,
Manning SW, Niu M, Reimer RW, Richards DA, Scott EM, Southon JR, Turney CSM,
van der Plicht J.
IntCal13 and MARINE13 radiocarbon age calibration curves 0-50000 years calBP
Radiocarbon 55(4). DOI: 10.2458/azu_js_rc.55.16947

Comments:
* This standard deviation (error) includes a lab error multiplier.
** 1 sigma = square root of (sample std. dev.^2 + curve std. dev.^2)
** 2 sigma = 2 x square root of (sample std. dev.^2 + curve std. dev.^2)
where ^2 = quantity squared.
[ ] = calibrated range impinges on end of calibration data set
0* represents a "negative" age BP
1955* or 1960* denote influence of nuclear testing C-14

NOTE:  Cal ages and ranges are rounded to the nearest year which
       may be too precise in many instances.  Users are advised to
       round results to the nearest 10 yr for samples with standard
       deviation in the radiocarbon age greater than 50 yr.
```

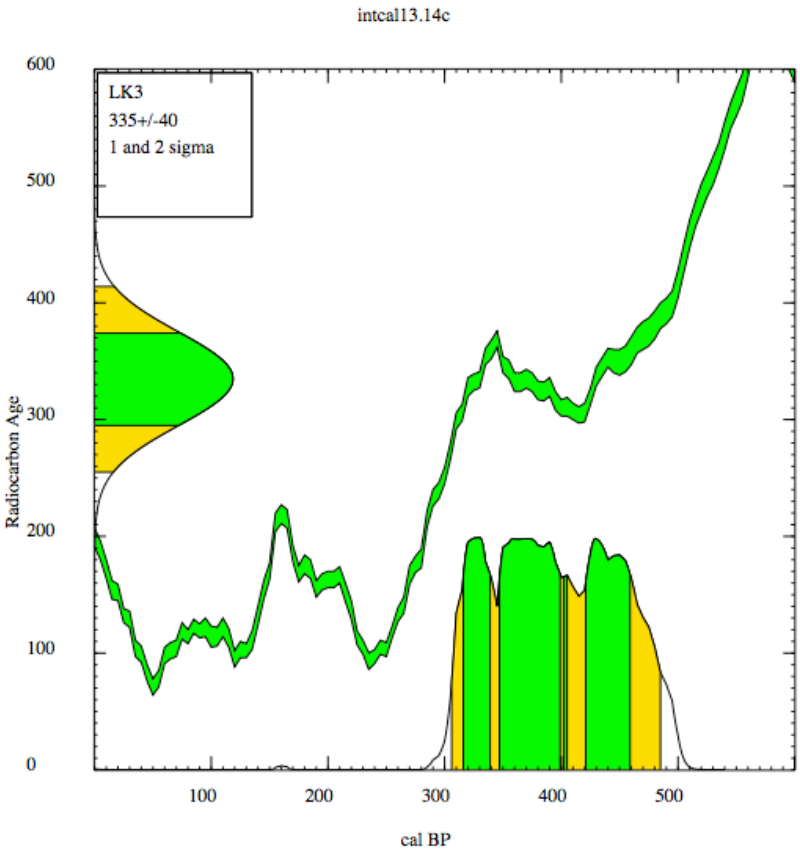

```
LK4
Lab Code
Sample Description
Radiocarbon Age BP    505 +/-   45
Calibration data set: intcal13.14c                  # Reimer et al. 2013
  % area enclosed       cal BP age ranges              relative area under
                                                     probability distribution
  68.3 (1 sigma)     cal BP 506 - 548                        1.000
  95.4 (2 sigma)     cal BP 492 - 562                        0.830
                            593 - 637                        0.170
  Median Probability:   532
```

References for calibration datasets:

Reimer PJ, Bard E, Bayliss A, Beck JW, Blackwell PG, Bronk Ramsey C, Buck CE Cheng H, Edwards RL, Friedrich M, Grootes PM, Guilderson TP, Haflidason H, Hajdas I, HattÃ© C, Heaton TJ, Hogg AG, Hughen KA, Kaiser KF, Kromer B, Manning SW, Niu M, Reimer RW, Richards DA, Scott EM, Southon JR, Turney CSM, van der Plicht J.
IntCal13 and MARINE13 radiocarbon age calibration curves 0-50000 years calBP
Radiocarbon 55(4). DOI: 10.2458/azu_js_rc.55.16947

Comments:

```
* This standard deviation (error) includes a lab error multiplier.
** 1 sigma = square root of (sample std. dev.^2 + curve std. dev.^2)
** 2 sigma = 2 x square root of (sample std. dev.^2 + curve std. dev.^2)
where ^2 = quantity squared.
[ ] = calibrated range impinges on end of calibration data set
0* represents a "negative" age BP
1955* or 1960* denote influence of nuclear testing C-14
```

NOTE: Cal ages and ranges are rounded to the nearest year which may be too precise in many instances. Users are advised to round results to the nearest 10 yr for samples with standard deviation in the radiocarbon age greater than 50 yr.

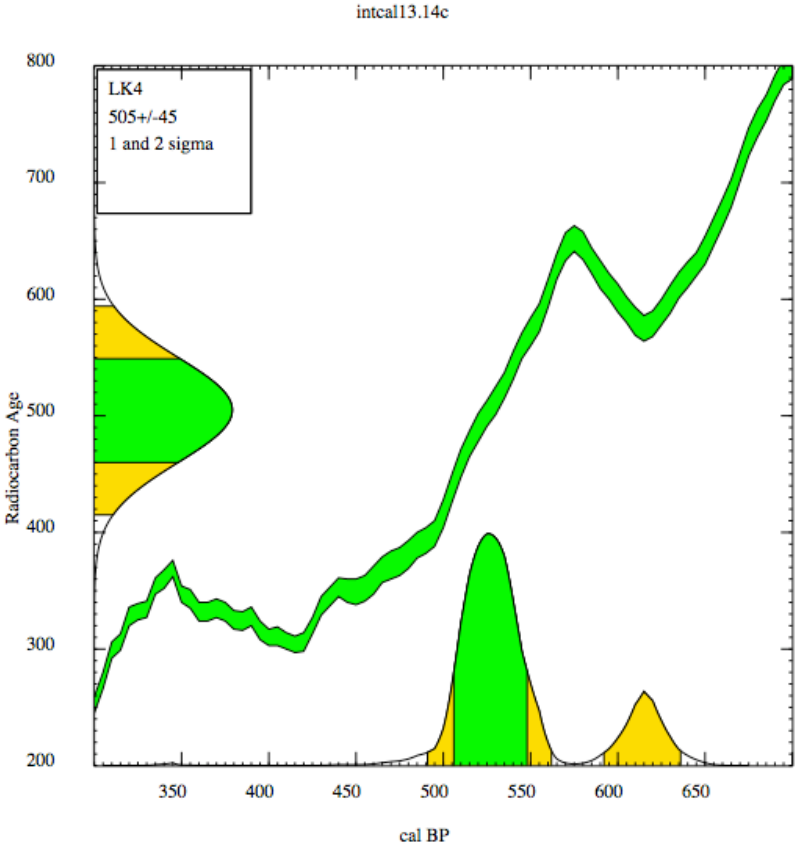

LK5
Lab Code
Sample Description
Radiocarbon Age BP 1605 +/- 30
Calibration data set: intcal13.14c # Reimer et al. 2013

% area enclosed	cal BP age ranges	relative area under probability distribution
68.3 (1 sigma)	cal BP 1417 - 1462	0.548
	1482 - 1493	0.091
	1517 - 1545	0.360
95.4 (2 sigma)	cal BP 1413 - 1554	1.000

Median Probability: 1482

References for calibration datasets:
Reimer PJ, Bard E, Bayliss A, Beck JW, Blackwell PG, Bronk Ramsey C, Buck CE
Cheng H, Edwards RL, Friedrich M, Grootes PM, Guilderson TP, Haflidason H,
Hajdas I, HattÃ© C, Heaton TJ, Hogg AG, Hughen KA, Kaiser KF, Kromer B,
Manning SW, Niu M, Reimer RW, Richards DA, Scott EM, Southon JR, Turney CSM,
van der Plicht J.
IntCal13 and MARINE13 radiocarbon age calibration curves 0-50000 years calBP
Radiocarbon 55(4). DOI: 10.2458/azu_js_rc.55.16947

Comments:
* This standard deviation (error) includes a lab error multiplier.
** 1 sigma = square root of (sample std. dev.^2 + curve std. dev.^2)
** 2 sigma = 2 x square root of (sample std. dev.^2 + curve std. dev.^2)
where ^2 = quantity squared.
[ ] = calibrated range impinges on end of calibration data set
0* represents a "negative" age BP
1955* or 1960* denote influence of nuclear testing C-14

NOTE: Cal ages and ranges are rounded to the nearest year which may be too precise in many instances. Users are advised to round results to the nearest 10 yr for samples with standard deviation in the radiocarbon age greater than 50 yr.

intcal13.14c

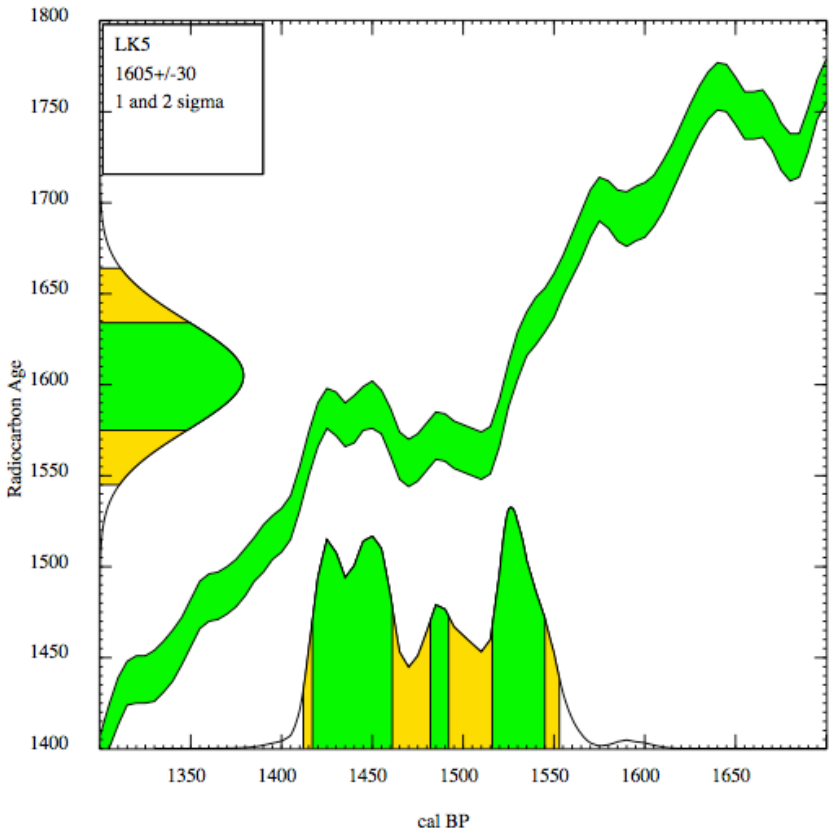

LK6
Lab Code
Sample Description
Radiocarbon Age BP 1300 +/- 70
Calibration data set: intcal13.14c # Reimer et al. 2013

% area enclosed	cal BP age ranges	relative area under probability distribution
68.3 (1 sigma)	cal BP 1175 - 1300	1.000
95.4 (2 sigma)	cal BP 1062 - 1332	1.000

Median Probability: 1222

References for calibration datasets:

Reimer PJ, Bard E, Bayliss A, Beck JW, Blackwell PG, Bronk Ramsey C, Buck CE Cheng H, Edwards RL, Friedrich M, Grootes PM, Guilderson TP, Haflidason H, Hajdas I, HattÃ© C, Heaton TJ, Hogg AG, Hughen KA, Kaiser KF, Kromer B, Manning SW, Niu M, Reimer RW, Richards DA, Scott EM, Southon JR, Turney CSM, van der Plicht J.
IntCal13 and MARINE13 radiocarbon age calibration curves 0-50000 years calBP
Radiocarbon 55(4). DOI: 10.2458/azu_js_rc.55.16947

Comments:
* This standard deviation (error) includes a lab error multiplier.
** 1 sigma = square root of (sample std. dev.^2 + curve std. dev.^2)
** 2 sigma = 2 x square root of (sample std. dev.^2 + curve std. dev.^2)
where ^2 = quantity squared.
[ ] = calibrated range impinges on end of calibration data set
0* represents a "negative" age BP
1955* or 1960* denote influence of nuclear testing C-14

NOTE: Cal ages and ranges are rounded to the nearest year which may be too precise in many instances. Users are advised to round results to the nearest 10 yr for samples with standard deviation in the radiocarbon age greater than 50 yr.

intcal13.14c

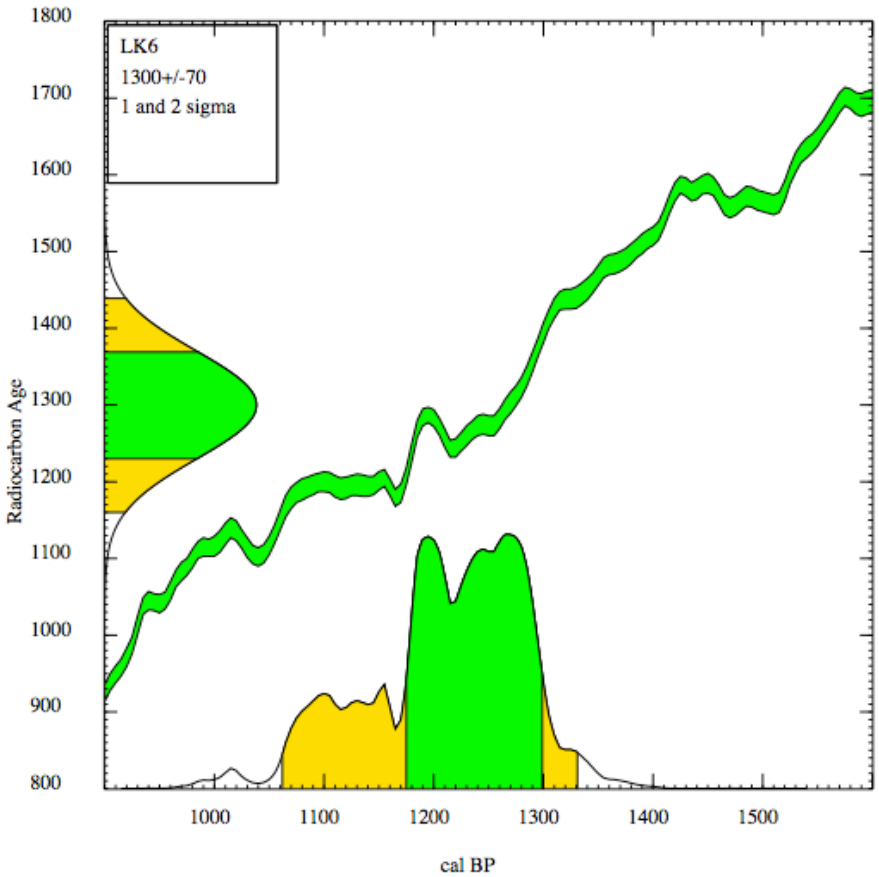

LK7
Lab Code
Sample Description
Radiocarbon Age BP 2240 +/- 100
Calibration data set: intcal13.14c # Reimer et al. 2013

% area enclosed	cal BP age ranges	relative area under probability distribution
68.3 (1 sigma)	cal BP 2125 - 2350	1.000
95.4 (2 sigma)	cal BP 1952 - 1958	0.002
	1974 - 1975	0.000
	1987 - 2492	0.981
	2600 - 2608	0.003
	2640 - 2679	0.014

Median Probability: 2235

References for calibration datasets:
Reimer PJ, Bard E, Bayliss A, Beck JW, Blackwell PG, Bronk Ramsey C, Buck CE
Cheng H, Edwards RL, Friedrich M, Grootes PM, Guilderson TP, Haflidason H,
Hajdas I, HattÃ© C, Heaton TJ, Hogg AG, Hughen KA, Kaiser KF, Kromer B,
Manning SW, Niu M, Reimer RW, Richards DA, Scott EM, Southon JR, Turney CSM,
van der Plicht J.
IntCal13 and MARINE13 radiocarbon age calibration curves 0-50000 years calBP
Radiocarbon 55(4). DOI: 10.2458/azu_js_rc.55.16947

Comments:
* This standard deviation (error) includes a lab error multiplier.
** 1 sigma = square root of (sample std. dev.^2 + curve std. dev.^2)
** 2 sigma = 2 x square root of (sample std. dev.^2 + curve std. dev.^2)
where ^2 = quantity squared.
[ ] = calibrated range impinges on end of calibration data set
0* represents a "negative" age BP
1955* or 1960* denote influence of nuclear testing C-14

NOTE: Cal ages and ranges are rounded to the nearest year which may be too precise in many instances. Users are advised to round results to the nearest 10 yr for samples with standard deviation in the radiocarbon age greater than 50 yr.

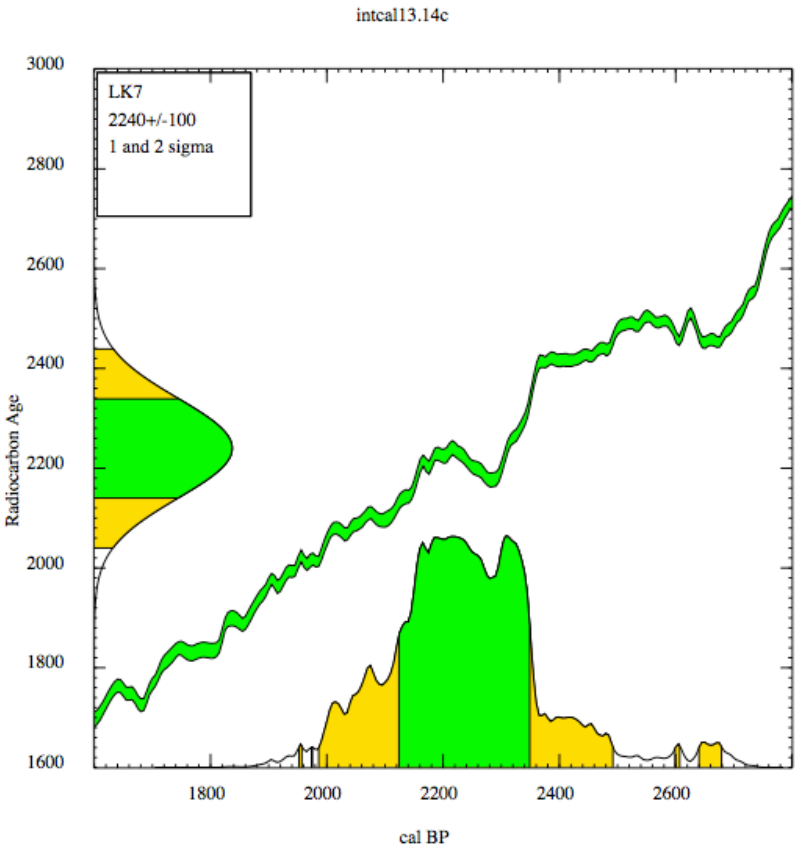

```
LK8
Lab Code
Sample Description
Radiocarbon Age BP    3060 +/-   60
Calibration data set: intcal13.14c                  # Reimer et al. 2013
  % area enclosed       cal BP age ranges               relative area under
                                                      probability distribution
  68.3 (1 sigma)      cal BP 3184 - 3190                      0.031
                             3208 - 3355                      0.969
  95.4 (2 sigma)      cal BP 3076 - 3097                      0.024
                             3103 - 3390                      0.976
  Median Probability:  3264

 References for calibration datasets:
Reimer PJ, Bard E, Bayliss A, Beck JW, Blackwell PG, Bronk Ramsey C, Buck CE
Cheng H, Edwards RL, Friedrich M, Grootes PM, Guilderson TP, Haflidason H,
Hajdas I, HattÃ© C, Heaton TJ, Hogg AG, Hughen KA, Kaiser KF, Kromer B,
Manning SW, Niu M, Reimer RW, Richards DA, Scott EM, Southon JR, Turney CSM,
van der Plicht J.
IntCal13 and MARINE13 radiocarbon age calibration curves 0-50000 years calBP
Radiocarbon 55(4). DOI: 10.2458/azu_js_rc.55.16947

Comments:
* This standard deviation (error) includes a lab error multiplier.
** 1 sigma = square root of (sample std. dev.^2 + curve std. dev.^2)
** 2 sigma = 2 x square root of (sample std. dev.^2 + curve std. dev.^2)
where ^2 = quantity squared.
[ ] = calibrated range impinges on end of calibration data set
0* represents a "negative" age BP
1955* or 1960* denote influence of nuclear testing C-14

NOTE:  Cal ages and ranges are rounded to the nearest year which
       may be too precise in many instances.  Users are advised to
       round results to the nearest 10 yr for samples with standard
       deviation in the radiocarbon age greater than 50 yr.
```

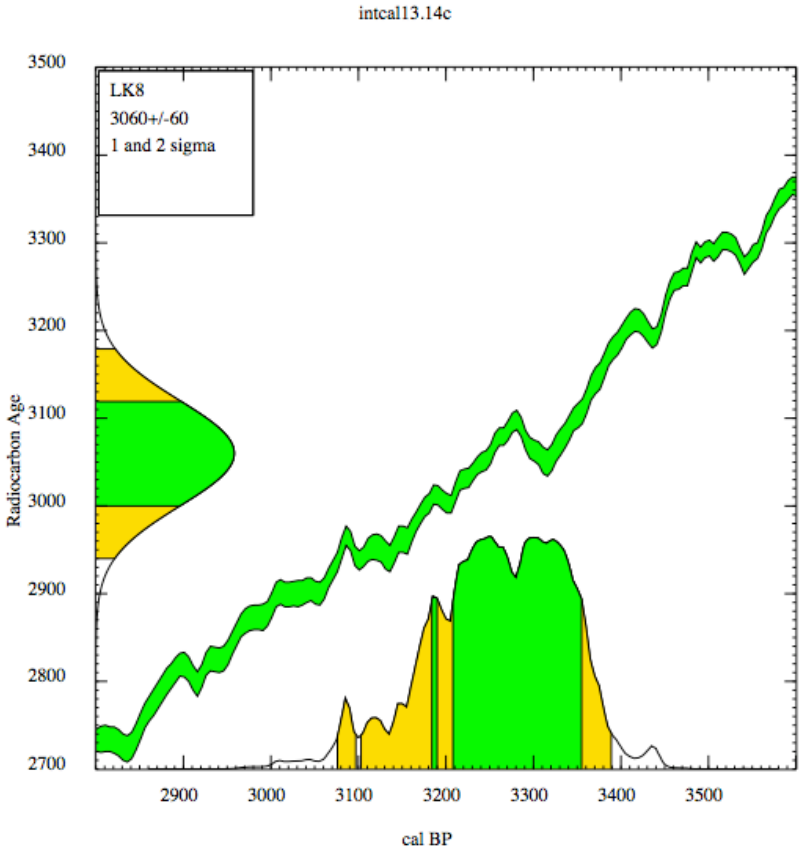

LK11
Lab Code
Sample Description
Radiocarbon Age BP 3605 +/- 40
Calibration data set: intcal13.14c # Reimer et al. 2013

% area enclosed	cal BP age ranges	relative area under probability distribution
68.3 (1 sigma)	cal BP 3865 - 3934	0.691
	3938 - 3971	0.309
95.4 (2 sigma)	cal BP 3779 - 3786	0.005
	3828 - 3996	0.940
	4037 - 4078	0.054

Median Probability: 3915

References for calibration datasets:
Reimer PJ, Bard E, Bayliss A, Beck JW, Blackwell PG, Bronk Ramsey C, Buck CE
Cheng H, Edwards RL, Friedrich M, Grootes PM, Guilderson TP, Haflidason H,
Hajdas I, HattÃ© C, Heaton TJ, Hogg AG, Hughen KA, Kaiser KF, Kromer B,
Manning SW, Niu M, Reimer RW, Richards DA, Scott EM, Southon JR, Turney CSM,
van der Plicht J.
IntCal13 and MARINE13 radiocarbon age calibration curves 0-50000 years calBP
Radiocarbon 55(4). DOI: 10.2458/azu_js_rc.55.16947

Comments:
* This standard deviation (error) includes a lab error multiplier.
** 1 sigma = square root of (sample std. dev.^2 + curve std. dev.^2)
** 2 sigma = 2 x square root of (sample std. dev.^2 + curve std. dev.^2)
where ^2 = quantity squared.
[ ] = calibrated range impinges on end of calibration data set
0* represents a "negative" age BP
1955* or 1960* denote influence of nuclear testing C-14

NOTE: Cal ages and ranges are rounded to the nearest year which
may be too precise in many instances. Users are advised to
round results to the nearest 10 yr for samples with standard
deviation in the radiocarbon age greater than 50 yr.

intcal13.14c